University of Calabria

Department of Pharmacy and Health and Nutrition Sciences (DFSSN)
Research Doctorate in Translational Medicine

CYCLE XXXVII

MESOPOROUS SILICA NANOPARTICLES FOR THE SELECTIVE DELIVERY OF DOXORUBICIN TO FOLATE RECEPTOR- EXPRESSING CANCER CELLS

S.S.D. MEDS-02/A General Pathology

Tutor

Prof. Diego Sisci

PhD Student

Dr. Camilla Longobucco

Coordinator

Prof. Stefania Catalano

STEFANIA CATALANO 08.05.2025 15:40:18 UTC

Table of Contents

Abstract

Breast and cervical cancers significantly impact women's health globally, with breast cancer accounting for approximately 2.3 million new cases annually. This highlights the urgent need for targeted therapeutic strategies that effectively eliminate tumor cells while preserving normal tissues. In this study, we developed a mesoporous silica-based nanodevice, FOL-MSN-DOXO, designed for the localized delivery of the chemotherapeutic agent doxorubicin (DOXO). This nanodevice utilizes the acidic tumor microenvironment for drug release via an acid-labile bond and incorporates folic acid (FOL) to enhance uptake by folate receptor-expressing cancer cells (FR+).

The efficacy of FOL-MSN-DOXO was evaluated through various *in vitro* assays, including fluorescence-activated cell sorting (FACS), growth assays, and ROS measurements, as well as immunostaining of dorsal root ganglia (DRG) cells from neonatal rats. Our results demonstrate that FOL-MSN-DOXO effectively induces apoptosis in FR+ cancer cells (e.g., HeLa and T-47D), while exhibiting minimal toxicity towards FR– normal cells (3T3-L1 and BJhTERT). Conversely, free DOXO exhibited significant toxicity across all tested cell lines. Notably, FOL-MSN-DOXO reduced neuronal toxicity compared to free DOXO, underscoring its neuroprotective potential.

In summary, FOL-MSN-DOXO offers a promising targeted drug delivery system that selectively induces cytotoxicity in FR+ cancer cells while sparing normal tissues. This approach mitigates the neurotoxic effects associated with doxorubicin, highlighting the efficacy and safety of folic acid-functionalized mesoporous silica nanoparticles in cancer treatment.

Introduction

Breast and cervical cancers represent two of the most prevalent malignancies affecting women globally, contributing significantly to cancer-related morbidity and mortality. According to the GLOBOCAN 2022 database, breast cancer is the most commonly diagnosed cancer worldwide, with approximately 2.3 million new cases reported, and it remains a leading cause of cancer-related deaths among women, accounting for around 685,000 fatalities annually. Cervical cancer, though less common, also presents a major global health challenge, with over 600,000 new cases and approximately 340,000 deaths recorded in the same period [1]. These alarming figures highlight the pressing need for more effective, safer, and targeted therapeutic strategies to manage and treat these cancers.

Among the chemotherapeutic agents available, doxorubicin (DOXO) remains a cornerstone of first-line treatment for a broad spectrum of solid tumors, including breast and cervical cancer [2]. This anthracycline antibiotic, originally isolated from *Streptomyces peucetius* var. *caesius* [3], exhibits potent antineoplastic activity. Its mechanism of action, though not fully elucidated, is primarily attributed to its ability to intercalate into DNA strands, thereby inhibiting the enzyme topoisomerase II [4, 5]. In addition, several studies have demonstrated that doxorubicin induces mitochondrial dysfunction by disrupting the integrity of the mitochondrial membrane, which results in an increased production of reactive oxygen species (ROS) [2, 6]. The increased production of ROS, which leads to oxidative stress, combined with the inhibition of DNA replication and repair mechanisms, contributes to the activation of regulated cell death pathways, particularly apoptosis in cancer cells [7, 8].

Despite its widespread clinical use, the therapeutic application of DOXO is constrained by a range of severe, dose-limiting toxicities. The most concerning is cardiotoxicity, which can progress to irreversible cardiomyopathy and congestive heart failure, especially when DOXO is co-administered with agents like trastuzumab or paclitaxel or used in conjunction with radiotherapy [9, 10]. In addition to its cardiotoxic effects, DOXO is associated with myelosuppression, which necessitates continuous monitoring of hematological parameters during therapy [11]. DOXO-induced side effects also include significant neurotoxicity, particularly affecting synaptic transmission and neurogenesis within the hippocampus [12, 13]. This neurotoxicity has become an increasing concern, as it not only impairs patient quality of life but may also persist long after the cessation of treatment.

In response to these challenges, various strategies have been explored to minimize toxicity while maintaining therapeutic efficacy. These include dose adjustment protocols [14, 15], the co-administration of cardioprotective agents such as dexrazoxane [16, 17], and the development of novel DOXO analogues with improved safety profiles [16, 18].

In recent years, nanotechnology has emerged as a transformative approach to overcoming the limitations of conventional chemotherapy. Drug delivery systems (DDSs) based on nanomaterials offer numerous advantages, including targeted delivery, controlled release, improved solubility, and enhanced pharmacokinetic and pharmacodynamic properties [19, 20]. Notably, DDSs can reduce off-target effects by directing therapeutic agents specifically to tumor sites, thus minimizing damage to healthy tissues. These systems also provide a protective environment that prevents premature drug degradation, ensuring the active compound reaches its intended target.

Numerous nanocarrier systems have been engineered to improve DOXO delivery. Among the most established are liposomal formulations such as Doxil®, LipoDox®, Myocet®, and ThermoDox®. Doxil®, the first FDA-approved nanomedicine in 1995, remains widely used for treating metastatic ovarian cancer, multiple myeloma, and AIDS-related Kaposi's sarcoma [21]. However, despite their improved safety profiles, these formulations still suffer from limitations such as suboptimal drug release, reduced bioavailability, and nonspecific distribution [22, 23].

To address these issues, research has increasingly focused on mesoporous silica nanoparticles (MSNs) as promising DDS platforms for DOXO. MSNs offer several advantageous features, including high surface area, large pore volume, and tunable pore sizes, which enable high drug loading capacity [24]. The surface of MSNs can be readily functionalized with various ligands to enhance cellular uptake and facilitate targeted delivery [25, 26]. Also, MSNs exhibit excellent biocompatibility and biodegradability, critical attributes for clinical applications [27].

For example, Peng et al. designed an MSN-hydroxyapatite hybrid nanocarrier, functionalized with oligo-hyaluronic acid (HA), to selectively target CD44 receptors. In vivo studies in tumor-bearing mice demonstrated superior therapeutic outcomes with this formulation compared to HA-coated variants, underscoring the importance of optimized targeting strategies [28]. Likewise, Bandyopadhyaya and colleagues engineered MSNs conjugated with amine groups and polyethylene glycol (PEG), further functionalized with folic acid (FA) or HA. These pH-responsive nanocarriers (MSN-NH2-DOXO-PEG-FA and MSN-NH2-DOXO-PEG-HA) not only inhibited tumor progression but also extended survival in preclinical models while reducing the adverse effects commonly seen with free DOXO [29].

Among the diverse approaches for stimuli-responsive drug release, pH-sensitive DDSs have gained considerable attention, mainly because tumors exhibit abnormal pH values that can be used to trigger drug release selectively. Cancerous tissues and intracellular compartments like endosomes and lysosomes typically exhibit lower pH values (pH 6.0–7.0 and pH 4.5–6.0, respectively) compared to the physiological pH of 7.4 [30, 31]. This pH differential can be exploited to achieve selective drug release at the tumor site, thereby enhancing therapeutic specificity. One of the most commonly used acid-sensitive linkages in DDSs is the hydrazone bond, which remains stable under neutral conditions but undergoes hydrolysis in acidic environments, triggering drug release [32-34].

DOXO's chemical structure features functional groups such as carbonyl, hydroxyl, and amino moieties that can be modified to form acid-labile linkages. Specifically, its hydroxymethylketone group can be converted into a hydrazone bond through a reaction with hydrazine derivatives. This hydrazone linkage forms the basis of numerous pH-sensitive DDSs, ensuring that DOXO is only released in the acidic intracellular environments of tumor cells while remaining stable in circulation.

Building on previous work by our group [35], in which a folate-functionalized MSN platform (FOL-MSN-BTZ) was successfully used to deliver bortezomib selectively to folate receptor-overexpressing multiple myeloma cells, we have developed a similar nanodevice for DOXO delivery: FOL-MSN-DOXO. In this system (**Fig.1**), folic acid is conjugated to the external surface of MSNs to serve as a targeting ligand, capitalizing on the high expression of folate receptors in many tumor types, including breast and cervical cancers [36]. Recent works demonstrate that folic acid binds selectively to folate receptors, which are overexpressed in a wide range of tumor cells compared to normal tissues, thereby enabling efficient and specific uptake of nanocarriers. This evidence

provides a robust rationale for employing folic acid-functionalized MSNs in targeted cancer therapy [37, 38].

Within the internal pore surfaces of FOL-MSN, DOXO is conjugated via an acid-labile hydrazone bond. This configuration ensures that the drug remains securely attached during systemic circulation and is only released upon encountering the acidic microenvironment of tumor cells. Consequently, this pH-sensitive design offers dual benefits: it protects normal tissues from cytotoxic exposure and enhances the accumulation of DOXO at the tumor site.

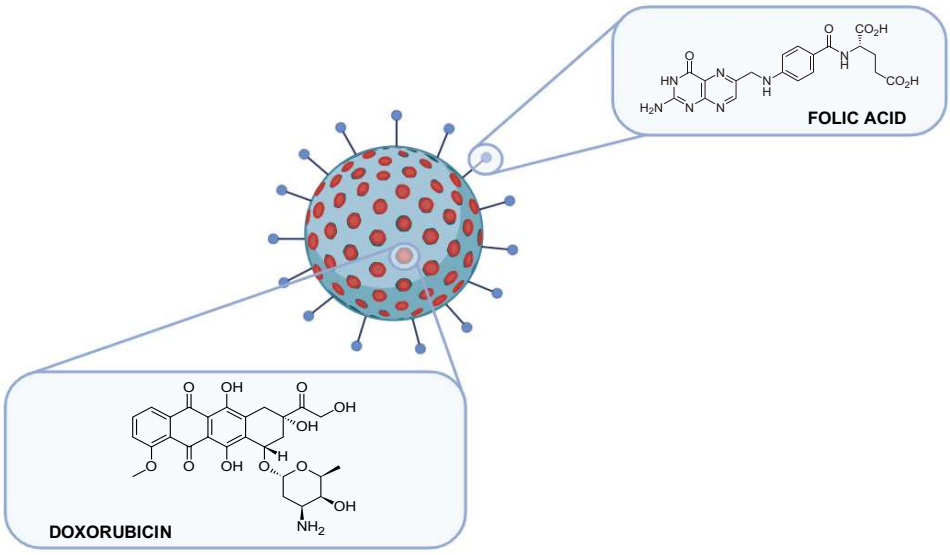

Figure 1. Structural Representation of the FOL-MSN-DOXO Nanosystem

Lastly, to better assess the therapeutic safety of this nanosystem, we evaluated the neurotoxicity profile of FOL-MSN-DOXO by studying its effects on dorsal root ganglia (DRG) neurons, a model system for peripheral neurotoxicity. Comparisons were made with free DOXO to determine whether the nanocarrier formulation could mitigate the

neurological side effects often observed with conventional chemotherapy. These findings underscore the potential of MSN-based nanodevices in improving the therapeutic index of DOXO while minimizing its adverse effects.

MATERIAL AND METHODS

2.1 Chemicals and reagents

Reagents were commercially available with analytical grade and used as purchased without further purification. Solvents were purified according to well-known laboratory methods and freshly distilled before use. Ultrapure water was distilled with the MilliQ® water, Millipore.

The following chemicals were obtained from Sigma Aldrich: neutral polyoxyethylene(10)octylphenyl ether (Triton X-100), tetraethyl orthosilicate (TEOS), (3-aminopropyl)triethoxysilane (APTES), folic acid (FOL), diisopropylcarbodiimide (DIC), doxorubicin hydrochloride (European Pharmacopoeia (EP) Reference Standard), hydrazine monohydrate, succinic anhydride, 4-dimethylaminopyridine (DMAP), HPLC grade water, and HPLC grade acetone.

Ethanol, diethyl ether, 1,4-dioxane, dimethylformamide (DMF), tetrahydrofuran (THF), trifluoroacetic acid (TFA), and acetic acid were purchased from VWR. Dimethyl sulfoxide (DMSO) and cyclohexane were sourced from Merck, while triethylamine (TEA) was obtained from Carlo Erba.

Minimum Essential Medium (MEM), Dulbecco's Modified Eagle's Medium (DMEM), Dulbecco's Modified Eagle's Medium (DMEM) high glucose, RPMI 1640 (1×) Medium, and Fetal Bovine Serum (FBS) were from Gibco™ (Life Technologies, Monza MB, Italy). Trypsin-EDTA solution (10×), L-glutamine, penicillin/streptomycin (pen/strep), D-glucose, HEPES, Sodium Pyruvate, Non-Essential Amino Acids, Insulin, and phosphate-buffered saline (PBS), as well as doxorubicin hydrochloride European Pharmacopoeia (EP) Reference Standard, were obtained from Sigma Aldrich (Merck Life Science, Milan, Italy).

2.2 Instruments

Thermogravimetric analysis (TGA) was carried out using a Netzsch STA 409 instrument between 20°C and 850 °C with a heating rate of 10 °C/min in air with a flow rate of 10 mL/min.

The zeta potential values of MSNs were measured using a Zetasizer ZS (Malvern-Panalytical, U.K.), at pH 7.1 (25.0 °C ± 0.1°C). The zeta potential values were calculated by the instrument software, using the Helmholtz–Smoluchosky equation.

N_2 adsorption−desorption isotherms at 77 K were collected using a Tristar II Plus 3.02 porosimeter (Micromeritics, Norcross, GA) under continuous adsorption conditions. A 300 UV-Vis Evolution spectrophotometer (Thermo Fisher Scientific, Waltham, MA, USA) was used to evaluate doxorubicin amount. Full absorption spectra of DOXO were measured in the range 200-700 nm, with the maximum absorption peak at 481 nm. Standard solutions with DOXO concentrations ranging from 0.5 ppm to 50 ppm were tested. Three parallel samples were measured to gain the average value.

^{1}H and ^{13}C NMR spectra were recorded on a Bruker Avance 300 instrument at 300 MHz and 75 MHz, respectively. Chemical shifts (δ) are reported in ppm. Coupling constants (*J*) are reported in Hertz (Hz).

2.3 SYNTHESIS OF FOLIC ACID-FUNCTIONALIZED MESOPOROUS SILICA NANOPARTICLES (FOL-MSN)

2.3.1 Synthesis of Mesoporous Silica Nanoparticles (MSNs)

The surfactant Triton X-100 (21 g) was dissolved in ultrapure water (230 g) at room temperature, with stirring for about four hours. To create two phases, a solution of TEOS

(22 g) in cyclohexane (9.8 g) was slowly added along the vessel (molar composition TEOS: Cyclohexane: Triton X-100: H2O was 1: 1.08: 0.32: 120, respectively).

The synthesis was carried out at room temperature. The upper phase was removed, and the resulting precipitate was collected by filtration and washed three times with ultrapure water. Finally, the sample was dried in the oven at 70 °C for 24 h, resulting in a white powder was obtained.

2.3.2 Synthesis of Amine Functionalized MSNs (AP-MSN)

The nanoparticles' surface was coated with aminopropyl groups using (3-aminopropyl)triethoxysilane (APTES).

A solution of APTES in ethanol (33 mL, 0.85 g/mL) was added to a suspension of MSNs (8 g) in ethanol (27.85 mL). The mixture was stirred at room temperature for 48 h. Afterward, the suspension was filtered and washed once with ethanol and twice with ultrapure water. The resulting sample (AP-MSN) was dried in an oven at 70° C for 24 h.

2.3.3 Synthesis of FOL-MSN

Folic acid (1.11 g, 2.51 mmol) was dissolved in DMSO (19.30 mL). Triethylamine (0.554 mL, 3.9 mmol), DIC (1.11 mL, 7 mmol), and AP-MSN (5.50 g) were added to the solution. The obtained suspension was stirred at room temperature for 40 h. Afterward, the mixture was filtered and washed sequentially with dimethylformamide, dioxane, diethyl ether, and ultrapure water. The resulting yellow powder (6.98 g) was dried and stored in sealed, light-protected containers.

To remove the surfactant within the pores, 1 g of the material was suspended in 0.33 L of ultrapure water at room temperature. The number of extractions required for complete surfactant removal was determined by monitoring the total mass loss of little amounts of

samples via thermogravimetric analysis (TGA) after each extraction step until a constant value was reached. Finally, the solution from the last extraction was filtered, and the obtained nanoparticles (FOL-MSN-EXT) were washed with 1,4-dioxane and dried at 45 °C overnight.

2.4 CONJUGATION OF DOXO TO FOL-MSN USING PH-SENTITIVE HYDRAZONE BOND - Synthesis of FOL-MSN-DOXO

2.4.1 Synthesis of FOL-MSN-APint

FOL-MSN-EXT was suspended in 1,4-dioxane at a concentration of 0.05 g/mL. APTES (2.2 g per gram of MSNs) was then added to the suspension. After stirring for 18 h, the mixture was filtered, and the solid residue was washed with 1,4-dioxane and THF. The resulting nanoparticles (FOL-MSN-APint) were dried overnight at 45 °C.

2.4.2 Synthesis of Succinic Acid Monohydrazide Linker

Succinic anhydride (1 g, 10 mmol) and DMAP (10 mg, 0,08 mmol) were dissolved in DCM (50 ml). Subsequently, a solution containing hydrazine monohydrate (0,320 g, 6 mmol) in DCM (10 ml) was added to the mixture dropwise under vigorous stirring at room temperature. After 10 h, the solvent was evaporated under reduced pressure, resulting in a white solid (1.1 g).

^{1}H NMR (300 MHz, DMSO-d6) δ: 11.80 (sbroad, 1H, COOH), 9.76 (s, 1H, CONH), 2.48-2.40 (m, 2H, (CH2COOH), 2.40-2.28 (m, 2H, (CH2CONHNH2).

^{13}C NMR (75 MHz, DMSO-d6) δ: 173.95, 170.36, 29.32, 28.51.

2.4.3 Synthesis of FOL-MSN-HYD

Succinic acid monohydrazide (0.218 g, 1.65 mmol) was dissolved in DMSO (20 mL), then DIC (0,256 mL, 1.65 mmol) and triethylamine (0,230 mL, 1.65 mmol) were added. After 1 h, a suspension of FOL-MSN-APint in DMSO (0.03 g/mL) was added to the reaction mixture. The reaction was stirred at room temperature for 24 h. Following this, the reaction mixture was filtered, and a second loading cycle was performed under the same conditions for another 24 h at room temperature. The mixture was then filtered, and the recovered powder was washed with DMSO and diethyl ether yielding FOL-MSN-HYD (1.65 g).

2.4.4 Drug Loading

A 20 mL solution of doxorubicin hydrochloride in DMSO (0.013 g/mL) was added to a 30 mL suspension of FOL-MSN-HYD in DMSO (0.017 g/mL). The pH was adjusted to approximately 5 by adding a few drops of acetic acid. The reaction mixture was stirred at room temperature under an inert atmosphere for 24 h. Subsequently, the nanoparticles were filtered and washed with DMSO. To achieve a higher drug loading, the resulting solid was resuspended in DMSO, and a second drug loading was carried out under the same conditions. Then, the reaction mixture was filtered and thoroughly washed with DMSO, dry dioxane, and dry dichloromethane. The obtained nanomaterial, FOL-MSN-DOXO, was stored in sealed containers at -20°C, under anhydrous conditions and protected from light. The amount of doxorubicin loaded (3.5 %) in FOL-MSN-DOXO was determined by TGA and UV-VIS spectroscopy (λabs = 481 nm).

2.5 Cell Cultures and Treatments

Human FR positive (FR+) cervix adenocarcinoma HeLa cells and T47D breast cancer cell line, as well as FR negative (FR−) normal mouse embryonic fibroblasts 3T3-L1 were purchased from ATCC, where they were authenticated. Additionally, the human SH-SY5Y and murine N2a neuroblastoma cell lines were also obtained from ATCC. Cells were stored according to supplier's instructions and used within 6 months after frozen aliquot resuscitations. Normal foreskin fibroblast BJhTERT cells were kindly provided by Michael Lisanti, University of Salford, Manchester (UK). Cells were purchased from ATCC and transferred to our laboratory at passage n = 3 and handled as described above. HeLa were cultured in MEM supplemented with 1% of non-essential amino acids, and 1% sodium pyruvate. T47D cells were grown in RPMI medium containing 2.5 g/ml glucose, 1% Na-pyruvate, 10 mM HEPES, and 0.2 U/ml insulin. BJhTERT cells were cultured in DMEM, while 3T3-L1 cells were maintained in DMEM high glucose supplemented with 10% Bovine Calf Serum (BCS, purchased from ATCC). N2a and SH-SY5Y were maintained in DMEM high-glucose. All media contained 10% FBS, except for 3T3-L1, 100 IU/mL pen/strep, and 0.2 mM L-Glutamine. Mycoplasma negativity was tested monthly with PlasmoTest (Invivogen, Aurogene, Rome, Italy). For cell treatments, MSNs were resuspended in serum-free media (SFM) using a magnetic stirrer. Subsequently, 50 μg of FOL-MSN-DOXO, equating to 2 μg/mL of free DOXO, was added to each well containing 10^5 cells in 1 mL of medium for a duration of 1 hour, based on results from titration experiments. Free DOXO (at a concentration of 2 μg/mL) was included as a positive control.

2.5.1 Fluorescence assisted cell sorting (FACS) analysis

HeLa and 3T3-L1 cells were seeded at 80% confluency on 60-mm dishes and incubated at 37°C in growth medium for 24 h. Subsequently, the cells were harvested using trypsin, washed with phosphate-buffered saline (PBS), and incubated in 100 µL of cold PBS with the primary antibody for 45 hours on ice (FOLR1 R&D, #MAB5646 for human HeLa cells and FOLR1 Invitrogen, PA5-116453, for murine 3T3-L1 cells). The cells were then washed twice with PBS and further incubated for 45 minutes with the secondary antibody (anti-Mouse IgG-TRITC Antibody, T5393, Sigma, for HeLa cells and anti-Rabbit IgG-FITC, F0382, both from Sigma Aldrich). The pellets were then washed twice, and fluorescence was measured using flow cytometry (CytoFLEX Beckman, Beckman Coulter, Milan, Italy). Data analysis was performed using CytExpert Beckman Coulter software (Beckman Coulter, Milan, Italy).

2.5.2 Cell Proliferation Assays

The effect of MSNs on cell proliferation was assessed using a trypan blue exclusion assay. Cells were seeded in triplicates for each condition in 12 well plates; specifically, HeLa cells were plated at a density of 50,000 cells/well, whereas 3T3-L1 cells were plated at a density of 70,000 cells/well. The cells were synchronized in SFM for 24 hours (4 hours were enough for 3T3-L1 cells, so to prevent detachment and morphological changes associated with prolonged starvation). After synchronization, the cells were treated as described above, then transferred to fresh growth medium (GM) supplemented with 1% serum. Cell viability was determined at 24, 48, and 72 hours using the Countess® II Automated Cell Counter (Invitrogen, Life Technologies) according to the manufacturer's instructions.

2.5.3 Transmission electron microscopy (TEM) and electron immunocytochemistry

For conventional TEM analysis, cells were seeded at a density of approximately 1×10^6 per 60-mm plate and treated as for the proliferation assay. All samples were routinely fixed, dehydrated, and resin-embedded using heat polymerization as previously described [35].

For indirect immunolabeling, grids were floated on drops of 1% bovine serum albumin (BSA) in PBS containing 0.02-M glycine at RT for 30 minutes to reduce nonspecific binding. Sections were then incubated with a mouse monoclonal antibody against FOLR1 (R&D, #MAB5646) at 277.15 K overnight. The grids were then transferred to 50 µL drops of secondary antibody conjugated to 10 nm gold particles for 1 h, at RT. Observations were performed under a Jeol JEM-1400 Plus electron microscope (Jeol Ltd, Tokyo, Japan) operating at 80 kV.

2.5.4 Spheroid formation assay

To generate individual spheroids, cells were seeded in 60-mm dishes under the same experimental conditions used for the proliferation assay. One-hour post-treatment, the cells were washed three times with PBS, harvested, and counted. Subsequently, 10^3 cells in 100 µL were plated in 96-well plates containing 100 µL of solidified 2% agar at the bottom of each well to prevent cell adhesion.

The diameter of each spheroid formed in the wells was photographed and measured at 24, 48, and 72 hours. At the conclusion of the experiment (72 hours), spheroid viability was assessed using the MTT assay [3-(4,5-dimethylthiazol-2-yl)-2,5-diphenyltetrazolium]. MTT (2 mg/mL, Sigma Aldrich) was added to each well, and the plates were incubated for 4 hours at 37°C. Following incubation, the content was

transferred to a new 96-well plate, and then the plate was spun at 1200 rpm for 5 minutes to remove the medium. Three spheroids were pooled and solubilized in a single well with 100 μL of DMSO (Sigma Aldrich), and the absorbance was measured at 570 nm.

2.5.5 Reactive oxygen species (ROS) assessment

ROS were quantified using the chloromethyl derivative of 2′,7′-dichlorodihydrofluorescein diacetate (CM-H2DCFDA, Thermo Fisher Scientific, Waltham, MA, USA), according to the manufacturer's recommendations. Briefly, HeLa (120,000 cells/well) and 3T3-L1 (170,000 cells/well) were seeded in 6-well plates, starved in serum-free medium (SFM), and treated with MSNs for 1 h. After treatment, the medium was replaced with fresh growth medium (GM), and the experiment was stopped after 72 h. The cells were then rinsed with PBS, harvested, resuspended in 5 μM CM-H2DCFDA, a fluorescent probe used as an indicator for ROS, in PBS, and incubated at 37 °C for 30–40 min. Subsequently, the stained cells were harvested by centrifugation, maintained in fresh medium, and incubated at 37 °C for 10 min. The cells were analyzed using flow cytometry (CytoFLEX, Beckman Coulter, Milan, Italy). Data analysis was performed using CytExpert Beckman Coulter software (Beckman Coulter, Milan, Italy).

2.5.6 Annexin V/PI assay

The Annexin V FITC & Propidium Iodide for Flow Cytometry (Invitrogen, Life Technologies, Milan, Italy) was used to perform the Annexin V/PI assay. Cells were seeded in 6-well plates following the same conditions as described for the ROS assay. After 1 hour of treatment, fresh GM was added, and the experiment was terminated at 24 hours for HeLa cells and at 48 hours for 3T3-L1 cells. At the end of the incubation, the

cells were collected with trypsin, centrifuged at 1000/1200 rpm for 5 min, and resuspended in PBS. Cells were resuspended in 1× binding buffer provided by the kit. 100 µL were transferred into a tube and incubated with 2 µL of Annexin V and 5 µL of PI for 15 min in the dark at room temperature. At the end of the incubation, 400 µL of Binding Buffer 1× was added to each tube, and the cells (or samples) were analyzed by flow cytometry (CytoFLEX, Beckman Coulter, Milan, Italy). Data analysis was performed using CytExpert Beckman Coulter software (Beckman Coulter, Milan, Italy).

2.5.7 TUNEL Assay

Apoptotic cells were identified by enzymatic labeling of DNA strand breaks using a Dead End Fluorimetric TUNEL (Terminal deoxynucleotidyl transferase dUTP nick end labeling) System (Promega, Milan, Italy) according to the manufacturer's instructions, in order to detect the DNA fragmentation, a hallmark of apoptosis. Briefly, 40,000 HeLa cells/well and 120,000 3T3-L1 cells/well in a 6-multiwell were seeded on coverslips and treated as previously described. After 72 h, coverslips were mounted on slides using Fluoromount mounting medium (Merck/Sigma-Aldrich) and observed under a fluorescence microscope (Olympus BX51, Olympus Italia, Milan, Italy). DAPI was used to counterstain the nuclei. Apoptotic cells were photographed at 10× magnification, using Proview™, through an Olympus camera system dp50 and then counted by Image J software (NIH, Bethesda, MD, USA).

2.5.8 Western Blotting (WB) Assay

HeLa and 3T3-L1 cells (800,000 cells/dish) were plated in 100 mm culture in GM and treated as previously described. After 72 h, cells were harvested and incubated 30 min on ice with cytoplasmic buffer containing 1 M sucrose, 1 M Hepes, 1 M KCl, 1 M MgCl2, 1 M EDTA, 1 M EGTA, Digitonin 10% and 200 mM PMSF. The cytoplasmic fraction was collected after centrifugation (13.000 rpm, 15 min, 4 °C). Intact mitochondria containing pellets were washed three times with PBS and incubated 30 min on ice with mitochondrial buffer (1 M Tris-HCL pH 7.4, 1 M EDTA, 1 M EGTA, TRITON X-100 plus inhibitors). The mitochondrial fraction was collected after centrifugation (13,000 rpm, 10 min, 4 °C).

30 μg (cytosolic extract) and 10 μg (mitochondrial extract) of protein lysates were run on an 10% and 13% polyacrylamide gel. For FR detection, total protein extracts were prepared by lysing the cells with RIPA buffer (R0278, Sigma Aldrich) supplemented with a protease inhibitor cocktail (aprotinin, phenylmethylsulfonyl fluoride, and sodium orthovanadate). Proteins were detected using specific antibodies: FOLR1 (#MAB5646, R&D Systems Inc., Minneapolis, MN, USA); Folate receptor alpha (PA5-116453 Invitrogen), PARP-1 (A11205 antibodies.com); caspase-3 (#9662), COX IV (4D11-B3-E8 #11967) and COX IV (3E11, #4850) all from Cell Signaling Technology, The Netherlands; Cytochrome C (sc-13560), GAPDH (sc-32233) and β-Actin (sc-69879) were from Santa Cruz Biotechnology, Inc. IRDye (LI-COR Corporate, NE, USA) were used as secondary Abs. Images were acquired with the Odyssey FC Imaging System (LI-COR Corporate).

2.5.9 Culture of dissociated DRGs, treatment, and immunofluorescence

Dorsal root ganglia (DRGs), the primary neurons in the sensory pathway, were isolated from neonatal Sprague Dawley rats at postnatal days 3–4 (P3–P4). Briefly, DRGs were dissected from all spinal segments, pooled, and collected in cold Hank's Balanced Salt Solution (HBSS). Residual spinal roots and attached nerves were carefully removed. DRGs were then enzymatically digested with collagenase IA (Sigma) for 35 minutes, followed by 7-minute digestion with TrypLE (Gibco). After digestion, DRGs were resuspended in complete culture medium (MM: DMEM/F12 supplemented with 10% fetal bovine serum [FBS], 1% penicillin/streptomycin [P/S], and 2.5 ng/µL nerve growth factor [NGF, Gibco). The cells were then mechanically dissociated using a 1,000 µL blue pipette tip and plated onto coverslips pre-coated overnight at 37°C with poly-L-lysine (Sigma, 20 µg/mL), followed by laminin (Sigma, 10 µg/mL) for 3 hours at 37°C.

Cells were seeded at a density of 100,000 cells per well in a 24-well plate and treated with either vehicle alone (FOL-MSN) or drug-loaded nanoparticles (FOL-MSN-DOXO) at doses equivalent to two different concentrations of free DOXO (0.5 µg and 1 µg/100,000 cells), which served as positive controls. One hour after treatment, the culture medium was replaced with fresh MM medium. After 72 hours, coverslips were fixed in 4% paraformaldehyde for 10 minutes, followed by blocking with 3% normal goat serum (NGS) for 1 hour at room temperature. Subsequently, coverslips were incubated overnight in a humid chamber with a rabbit anti-S100A1 (Z0311, DAKO) and a mouse anti-β-III-Tubulin (AB7751, Abcam) primary antibodies, S100A1 being a marker for Schwann cells (Sc) and β-III-Tubulin a neuronal marker. Alexa Fluor 488-(A21202, Invitrogen) and 647-(A31573, Invitrogen) conjugated secondary antibodies were used for the respective primaries and incubated for 1 hour at room temperature. Finally, coverslips

were counterstained with DAPI (D9542, Sigma) and mounted with Mowiol (81381, Sigma). Images were acquired from Leica DMI8 inverted and analyzed using ImageJ.

Results and Discussion

3.1 Synthesis and characterization of FOL-MSN-DOXO prototype

We achieved the development of the mesoporous silica-based nanosystem, FOL-MSN-DOXO, using MSU-type mesoporous silica nanoparticles.

The antineoplastic drug doxorubicin was anchored to the nanocarrier pore walls through an acid-sensitive hydrazone bond using a hydrazide-containing linker. The MSU-type mesoporous silica nanoparticles were obtained through a biphasic synthetic procedure carried out at room temperature, without the use of a mineralizing agent. We employed tetraethyl orthosilicate (TEOS) as the silica source and the surfactant Triton X-100 as structure-directing agent.

TEM and SEM analyses (**Fig. 2**) were performed on nanoparticles to examine their morphology. The results revealed that MSNs exhibited a uniform diameter size ranging from 80 to 120 nm and showed a porous texture consistent with mesoporous silica materials.

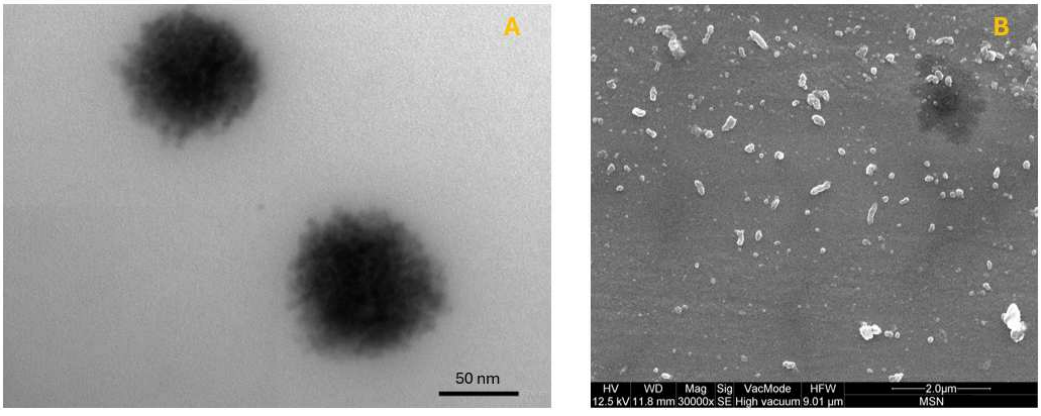

Figure 2. TEM (A) and SEM (B) micrographs of starting MSNs.

The external surface of as-synthesized MSNs was firstly functionalized with (3-Aminopropyl)triethoxysilane (APTES), resulting in amine-functionalized nanoparticles (AP-MSN). Then, folic acid (FOL), the targeting molecule, was covalently conjugated to the nanoparticles (FOL-MSN) through the formation of amide bonds between the amino groups of AP-MSN and the carboxylic function of folic acid (**Scheme 1**).

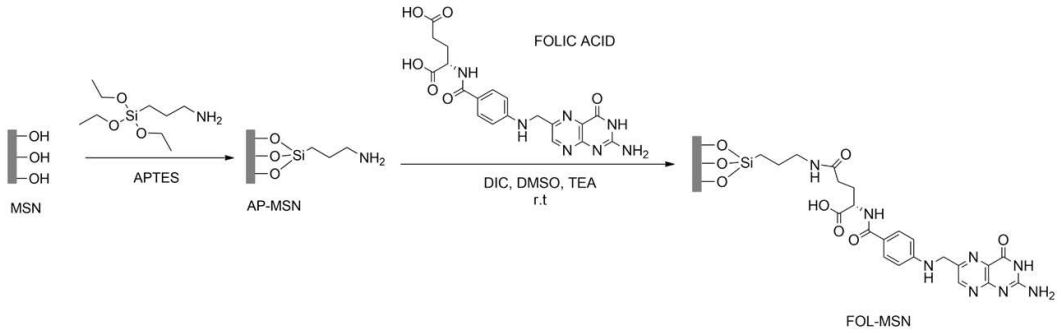

Scheme 1. Synthesis of FOL-MSN.

Thermogravimetric analysis of the sample before and after functionalization with FOL showed an increment of the organic compound mass on the sample by 12.20 %.

Importantly, to prevent a substantial reduction in pore volume, MSNs were externally functionalized before surfactant extraction. This approach ensured that a significant pore volume was maintained after surfactant removal, with the folic acid targeting molecule predominantly anchored on the external surface, thereby facilitating efficient drug loading.

Surfactant within the pores of FOL-MSN was then efficiently removed by solvent extraction using ultrapure water, resulting in FOL-MSN-EXT.

The next steps involved synthesizing a hydrazide-functionalized linker and inserting it into the pores of the extracted FOL-MSN system (FOL-MSN-EXT). This process is crucial for anchoring DOXO via an acid-sensitive hydrazone bond.

First, the inner pores of FOL-MSN-EXT were modified with amino groups by grafting APTES, resulting in FOL-MSN-APint. Next, a hydrazide-containing linker (SAH) was prepared by reacting succinic anhydride with hydrazine monohydrate at room temperature. This linker was incorporated into FOL-MSN-APint by forming an amide bond with the amino groups on the pore walls, using DIC (N,N′-Diisopropylcarbodiimide) as the condensing agent and triethylamine (TEA) as the base (**Scheme 2**). Finally, DOXO was conjugated to the hydrazide-modified nanoparticles (FOL-MSN-HYD) via a hydrazone bond between the hydrazide's amino group and DOXO hydroxymethyl ketone, creating FOL-MSN-DOXO (**Scheme 2**).

The amount of drug loaded (3.5 %) in FOL-MSN-DOXO was determined by thermogravimetric analysis (TGA) and UV-VIS analysis (λabs = 481 nm).

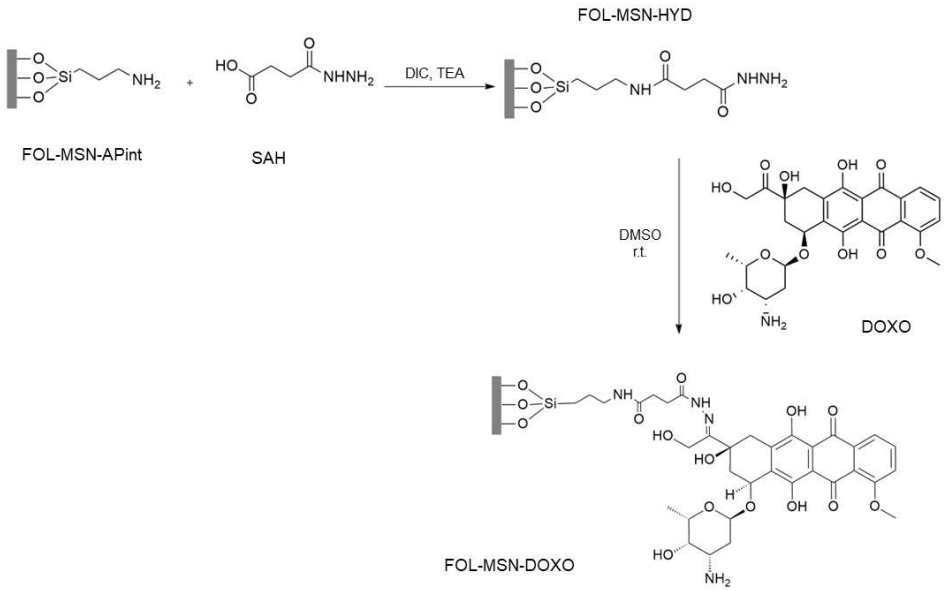

Scheme 2. Synthesis of FOL-MSN-DOXO.

The N_2 adsorption-desorption isotherms for all synthesized MSN systems exhibited type IV behaviour as shown in **Figure 3**. According to IUPAC classification, this confirms the mesoporous feature of the materials.

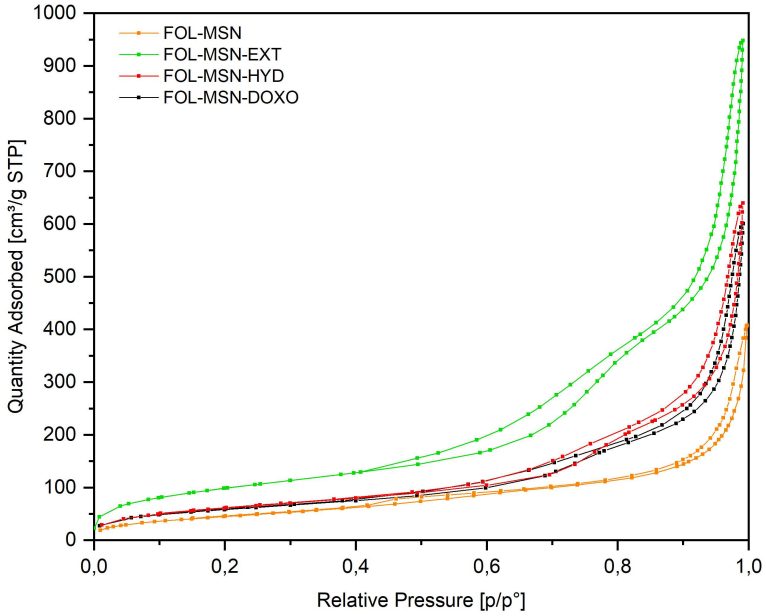

Figure 3. Nitrogen adsorption-desorption isotherms of FOL-MSN (orange), FOL-MSN-EXT (green), FOL-MSN-HYD (red) and FOL-MSN-DOXO (black).

The BET (Brunauer-Emmett-Teller) surface area and pore volume values, determined using the BJH (Barrett-Joyner-Halenda) method, are presented in **Table 1**. The removal of surfactant from the inner pores of FOL-MSN led to an increase in the BET surface area, from 170 m^2/g before extraction to 364 m^2/g for FOL-MSN-EXT. Similarly, the pore volume increased to 0.89 cm^3/g in the extracted FOL-MSN. However, subsequent surface modification resulted in a progressive decrease in both BET surface area and pore volume. Specifically, the BET surface area decreased to 212 m^2/g and the pore volume decreased to 0.49 cm^3/g in the FOL-MSN-DOXO sample.

Sample	BET Surface area [m^2/g]	Pore volume [cm^3/g]
FOL-MSN	170	0.32
FOL-MSN-EXT	364	0.89
FOL-MSN-APint	295	0.71
FOL-MSN-HYD	226	0.57
FOL-MSN-DOXO	212	0.49

Table 1. BET surface area and pore volume values at P/P^0= 0.96 of the MSN systems obtained in the FOL-MSN-DOXO development process.

The zeta potential values for MSNs, FOL-MSN-APint, FOL-MSN-HYD and final FOL-MSN-DOXO were determined and are shown in **Table 2**. The MSNs exhibited a negative zeta potential of -30.2 mV due to the negatively charged silanol groups on their external surface.

Sample	Zeta potential [mV]
MSN	-30.2
FOL-MSN-APint	+18.4
FOL-MSN-HYD	+16.9
FOL-MSN-DOXO	+39.9

Table 2. Zeta potentials of MSNs, FOL-MSN-APint, FOL-MSN-HYD and FOL-MSN-DOXO samples.

FOL-MSN-APint showed a positive zeta potential of +18.4 mV, which is attributed to the positively charged aminopropyl groups attached to the internal surfaces of the nanoparticles when suspended in water. Functionalization with the hydrazide linker

resulted in a similar zeta potential of +16.9 mV. After encapsulation of DOXO, the zeta potential of FOL-MSN-DOXO reached the value of +39.9 mV, due to the DOXO loading. This value is consistent with the protonated amino group attached to the pyran moiety of DOX. The positive zeta potential of FOL-MSN-DOXO indicates a higher potential for cellular uptake. This is due to the electrostatic attraction between the positively charged nanoparticles and the negatively charged cell membrane [39].

A series of experiments were conducted at different pH values to study the pH dependence of doxorubicin release from the nanosystem. Buffer solutions with pH values of 7.4 (mimicking systemic circulation), and 5 (mimicking the tumor microenvironment), were used as release media.

In each experiment, 10 mg of FOL-MSN-DOXO were dispersed in 15 mL of buffer solution at the desired pH and stirred at room temperature. After 24 hours, the suspension was filtered and centrifuged, and the supernatant was collected for analysis. The DOXO content in the supernatant was measured using UV-Visible spectroscopy at an absorbance of 481 nm. The drug concentration was determined using standard calibration curves for DOXO UV absorbance at each pH level.

The results, shown in **Figure 4**, indicate that pH significantly affects DOXO release. At pH 7.4, only 7% of DOXO was released, suggesting a slow hydrolysis and a good retention of DOXO within the MSN-based nanosystem. At pH 5, corresponding to the acidic tumor environment, 43% of DOXO was released after 24 hours, demonstrating the pH-responsive behaviour of the nanovehicle.

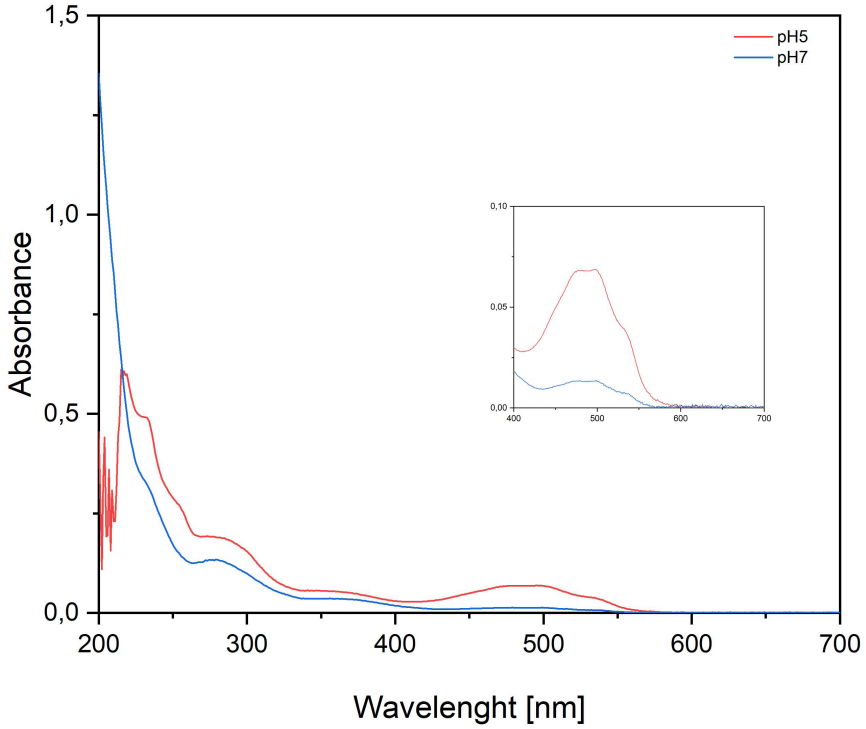

Figure 4. UV-Vis analysis of DOXO release after 24 h, at pH 7.4 (blue) and pH 5 (red). The insert box shows a zoom of the region between 400 nm and 700 nm.

3.2 *In vitro* biocompatibility, antitumor efficacy and safety of FOL-MSN-DOXO

The selectivity of the FOL-MSN-DOXO nanovehicle toward FR-expressing cells was assessed on HeLa and T-47D cells, chosen as FR-positive tumor cell models, and on 3T3-L1 and BJhTERT cells, as FR-negative normal cell models. This selection was supported by FACS analysis (**Fig. 5A**) and WB analysis (**Fig. 6A**), which demonstrated a significantly higher folate receptor expression in tumor cells compared to normal cells. The impact of MSNs on cell proliferation was then assessed in FR-positive HeLa and T-47D cell lines, revealing that FOL-MSN-DOXO effectively induces cell death in these tumor cells, with an effect comparable to that of the free drug. In contrast, the FR-negative cell lines 3T3-L1 and BJhTERT only exhibited cell death in response to DOXO alone (**Fig. 5B** and **Figure 6B**). To better simulate the *in vivo* environment, the impact of MSNs

was assessed on 3D spheroids (**Fig. 5C**). HeLa spheroids treated with FOL-MSN-DOXO exhibited a significantly smaller diameter compared to both the control group and those treated with FOL-MSN. This effect was comparable to that observed with DOXO, showing similar disaggregation and cellular dispersion around the spheroid core, thus effectively interfering with spheroid formation, mirroring the efficacy of the free drug. Additionally, treatment with FOL-MSN-DOXO resulted in a significant reduction in cell viability of over 50%, comparable to the effects observed with the free drug. Notably, in 3T3-L1 spheroids, only the free DOXO induced a significant decrease in spheroid diameter and reduced cell viability by approximately 40%, while FOL-MSN-DOXO showed no harmful effects on normal cells (**Fig. 5C**).

TEM observations corroborated these findings, demonstrating that the uptake of FOL-MSN-DOXO nanovehicle occurs exclusively in FR+ HeLa and T-47D cells, whereas it fails to enter FR- 3T3-L1 and BJhTERT cells (**Fig. 5D** and **Figure 6C**). Moreover, colloidal gold labeling for the FR showed that FOL-MSN-DOXO entry into HeLa cells occurs via FR-mediated endocytosis (**Fig. 5E**), confirming the high selectivity of our FOL-targeted MSNs toward FR-expressing cells [35, 40]

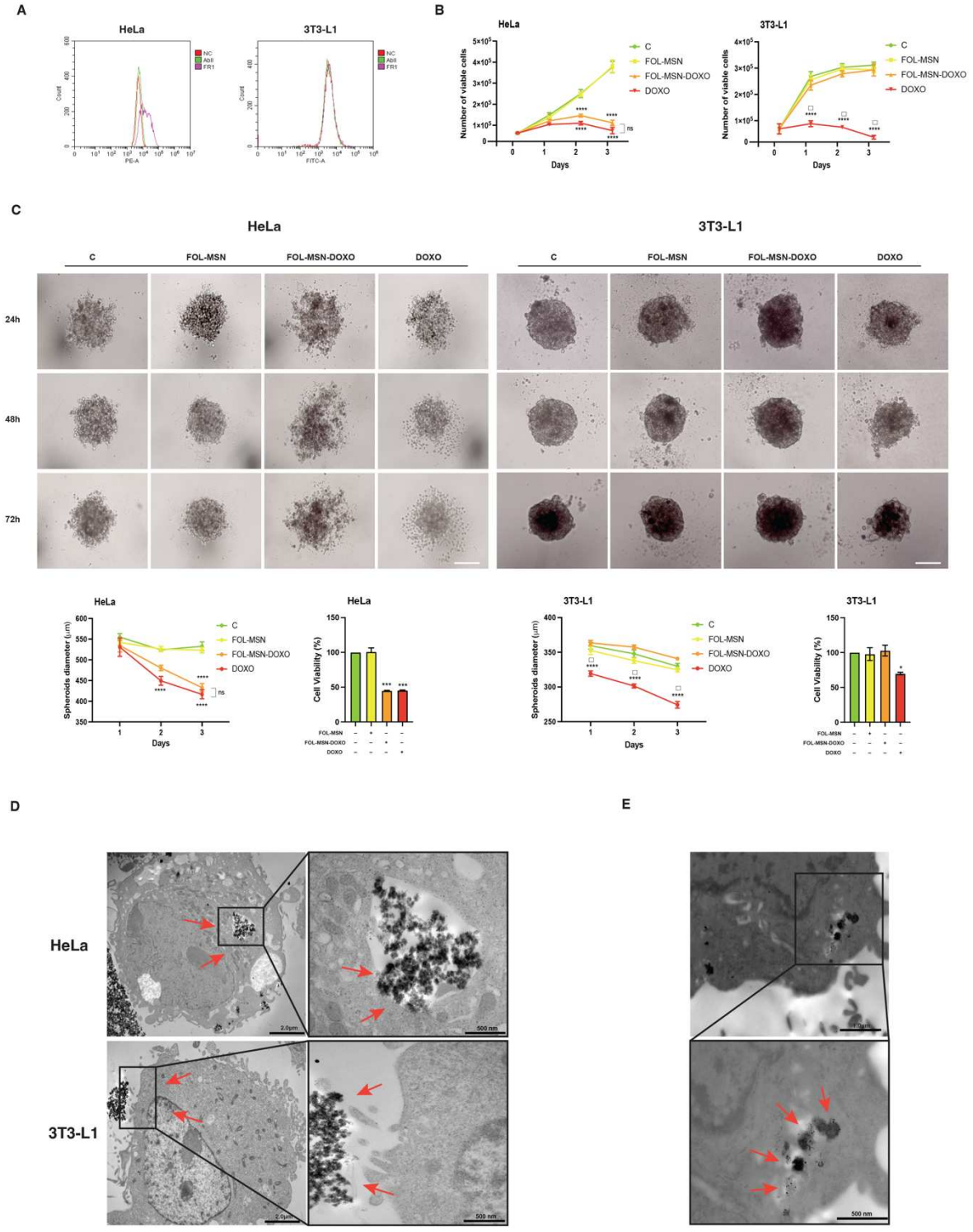

Figure 5: FOL-MSN-DOXO kills FR+ cancer cells but not FR- normal cells. A) FR expression was assessed by FACS analysis in HeLa and 3T3-L1 cells. Samples were prepared as described in *Materials and Methods* and analyzed by measuring the relative fluorescence intensity of FITC per cell (magenta) in the PE-A (HeLa) and FITC-A (3T3-L1) channels. Data were normalized against an untreated control (red) and corrected for secondary antibody autofluorescence (green). The results shown are representative of

three independent experiments. B) FOL-MSN-DOXO induces death in FR+ HeLa cells but not in FR- 3T3-L1 normal cells. Cells were treated for 1h with FOL-MSN-DOXO or left untreated (C = control). FOL-MSN was used as negative control and the free drug DOXO as positive control. Values represent the mean ± SEM of three independent experiments performed in triplicate (**** $p < 0.0001$ vs. control and FOL-MSN; ▢ **** $p < 0.0001$ vs. all other groups). C) Representative pictures of spheroids (a single spheroid/well) from the HeLa and 3T3-L1 spheroid cultures grown on agar-coated plates. Cells were pretreated for 1 hour with FOL-MSN, FOL-MSN-DOXO, free DOXO, or left untreated (Control). Scale bar: 400 µm. Spheroid diameter was quantified over 24, 48, and 72 hours using the Proview™ software; cell viability was evaluated using the MTT assay at 72 hours. Values represent the mean ± SEM of three independent experiments performed in triplicate. **** $p \leq 0.0001$ vs. control and FOL-MSN; *** $p < 0.001$ vs. control and FOL-MSN; ▢ **** $p < 0.0001$ vs. all other groups; *$p<0.05$ vs. all other groups. D) HeLa and 3T3-L1 were processed for TEM analysis. MSNs are indicated by red arrows. Images were taken at 3,000x magnification (scale bars: 2 µm, left panels) and 15,000x magnification (scale bars: 500 nm, right panels). E) Colloidal-gold immunocytochemistry for FRα (black dots indicated by arrows) in HeLa cells exposed to FOL-MSN-DOXO for 1 hour. The sequestration of FOL-MSN-DOXO nanoparticles in FRα-immunopositive intracellular vesicles is shown. Images were taken at 10,000x magnification, with scale bars at 1 µm (upper panel), and at 20,000x magnification, with scale bars at 500 nm (lower panel).

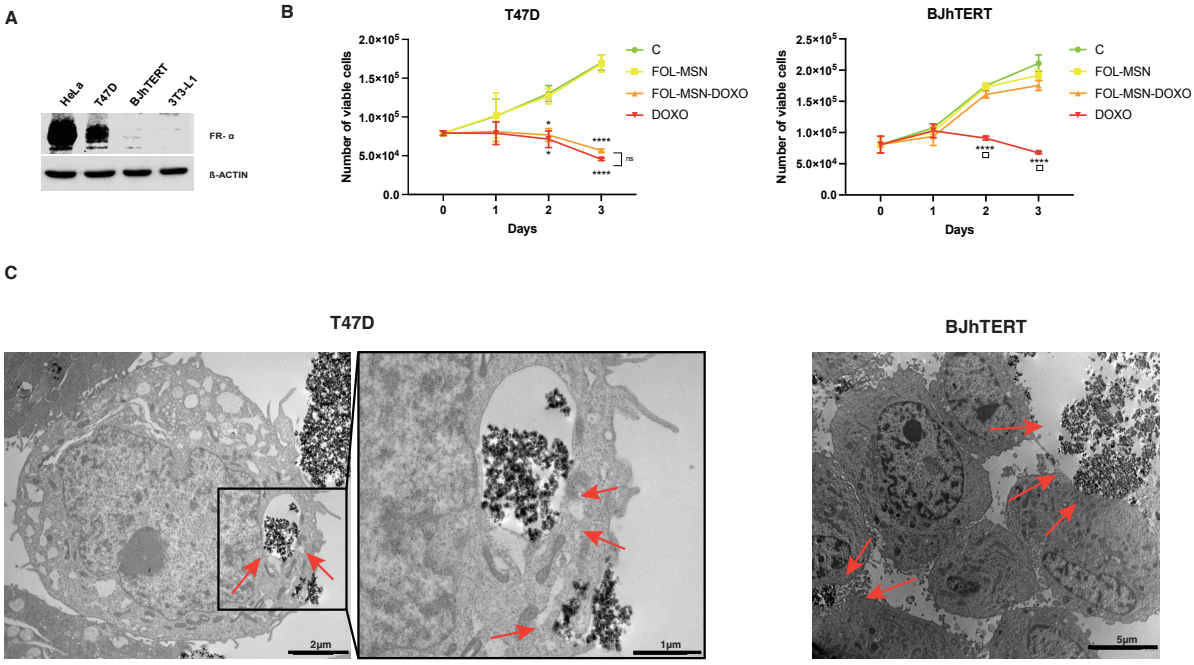

Figure 6: A) 30 µg of proteins (for FR-α detection) from total lysates of indicated cell lines were loaded and subjected to WB analysis. β-actin was used as loading control. **B**) FOL-MSN-DOXO induces death in FR+ T47D breast cancer cells but not in FR- BJhTERT normal cells. Cells were treated for 1h with FOL-MSN-DOXO or left untreated (C = control). FOL-MSN was used as a negative control and the free drug

DOXO as a positive control. Values represent the mean ± SEM of three independent experiments performed in triplicate. * $p < 0.05$ vs. control and FOL-MSN; **** $p < 0.0001$ vs. control and FOL-MSN; ▢**** $p < 0.0001$ vs. all other groups. **C**) T47D and BJhTERT were treated with FOL-MSN-DOXO for 1 hour and then processed for TEM analysis, as described in Materials and Methods. MSNs are indicated by red arrows. For T47D, images were acquired at 3000× magnification (scale bar: 2 μm) and 8000× magnification (scale bar: 1 μm). For BJhTERT, the representative image was taken at 1500× magnification (scale bar: 5.0 μm).

Doxorubicin primarily acts by inhibiting topoisomerase II, but it also disrupts mitochondrial homeostasis and triggers the production of ROS, resulting in oxidative stress and cellular damage[2, 6]. This cascade of events activates intracellular signaling pathways, leading to the release of cytochrome c and caspase activation, ultimately culminating in the apoptosis of tumor cells [2, 7, 8]. Therefore, the apoptotic pathway induced by doxorubicin has been investigated.

First, the impact of FOL-MSN-DOXO on ROS production has been compared to that of the free drug. Additionally, the effect of FOL-MSN alone on cellular oxidative homeostasis was investigated. As expected, both FOL-MSN-DOXO and free DOXO led to comparable levels of ROS production in FR+ HeLa cells (**Fig. 7A**).

Apoptosis is characterized by a series of distinctive morphological changes, including chromatin condensation and structural and functional cell membrane alterations, such as the externalization of phosphatidylserine[41, 42]. To further investigate these changes, membrane modifications were analyzed in HeLa cells after 24 hours of treatment with FOL-MSN, FOL-MSN-DOXO, or free doxorubicin. Annexin V assay (**Figure 7B**) revealed that HeLa cells treated with FOL-MSN-DOXO exhibited a notable apoptosis rate of 94.59%, indicating a rapid progression into both early and advanced stages of apoptosis. In contrast, cells treated with free DOXO demonstrated an apoptosis rate of 89.14%, predominantly in the early stage. The control and FOL-MSN-treated groups

displayed significantly lower apoptosis rates, at 21.55% and 21.6%, respectively. To further substantiate the induction of apoptosis, a TUNEL assay was conducted, demonstrating that both FOL-MSN-DOXO and free DOXO elicit comparable rates of apoptosis in FR+ HeLa tumor cells (**Figure 8A**). Moreover, the translocation of cytochrome c (Cyt c) from the mitochondria to the cytoplasm—an essential step in initiating the intrinsic apoptotic pathway—was observed in both FOL-MSN-DOXO and free DOXO-treated samples. Additionally, the cleavage of caspase-3 and its endogenous substrate, poly(ADP-ribose) polymerase (PARP-1), was evident (**Figure 7C**), further confirming the activation of the apoptotic cascade.

The same experiments were conducted using the normal FR-, 3T3-L1 cell line, demonstrating a notable ROS induction exclusively in cells treated with free DOXO (**Figure 7A**). Results from the Annexin V, TUNEL, and Western Blot assays (**Figures 7 B-C; Fig. 8A**) validated that apoptosis was induced only in the free DOXO-treated condition, whereas FOL-MSN-DOXO treatment did not activate apoptosis.

Similar results were obtained in other FR+ (T-47D) and FR- (BJhTERT) cell lines (**Figures 8B-C**), confirming the remarkable selectivity of our MSN-bound doxorubicin toward tumor cells compared with free doxorubicin.

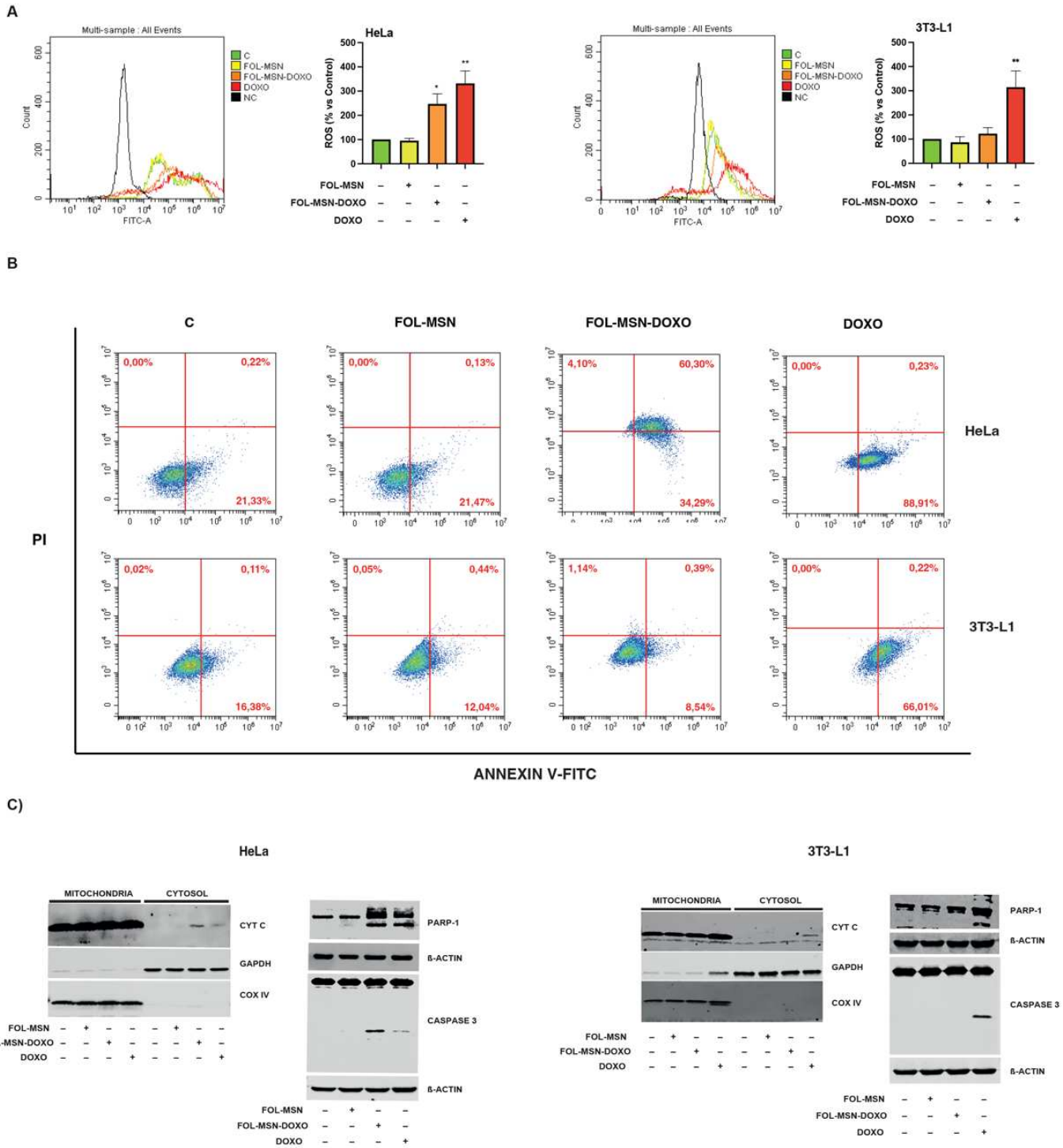

Figure 7: FOL-MSN-DOXO triggers apoptosis only in FR+ cancer cells. FR+ HeLa cancer cells and FR- 3T3-L1 normal cells were treated with FOL-MSN, FOL-MSN-DOXO, and free DOXO (positive control); untreated cells served as the negative control. **A**) Intracellular ROS levels have been detected. Representative images of the cytofluorimetric analysis (left panel), with the histogram (right panel) showing

mean values. Data are presented as mean ± SEM of three independent experiments performed in triplicate. Fluorescence intensity was normalized to the number of viable cells and expressed as a percentage relative to the negative control. Histograms represent the mean ± SEM of three independent experiments, each performed in triplicate. Data are shown as probe fluorescence normalized on viable cell number and expressed as a percentage vs. negative control. * $p \leq 0.05$, ** $p \leq 0.01$ vs. control and FOL-MSN; **$p \leq 0.01$ vs. all other groups. **B**) As detailed in Materials and Methods, cells were subjected to Annexin V assay after 24 (HeLa) and 48 hours (3T3-L1) from treatment. Apoptosis was assessed by flow cytometry. The four quadrants represent living cells (lower left, AnnexinV-/PI-), early apoptotic (lower right, Annexin V+/PI-), late apoptosis (upper right, Annexin V+/PI+), or necrotic (upper left, Annexin V-/PI+) stages. Values represent the percentages of each quadrant. **C**) Cells were treated as in (A), and mitochondrial and/or cytosolic fractions were extracted and subjected to WB analysis to assess the expression of the indicated apoptotic markers. β-Actin and GAPDH were used as loading controls; COX IV was used as a mitochondrial marker to assess the quality of protein fractionation.

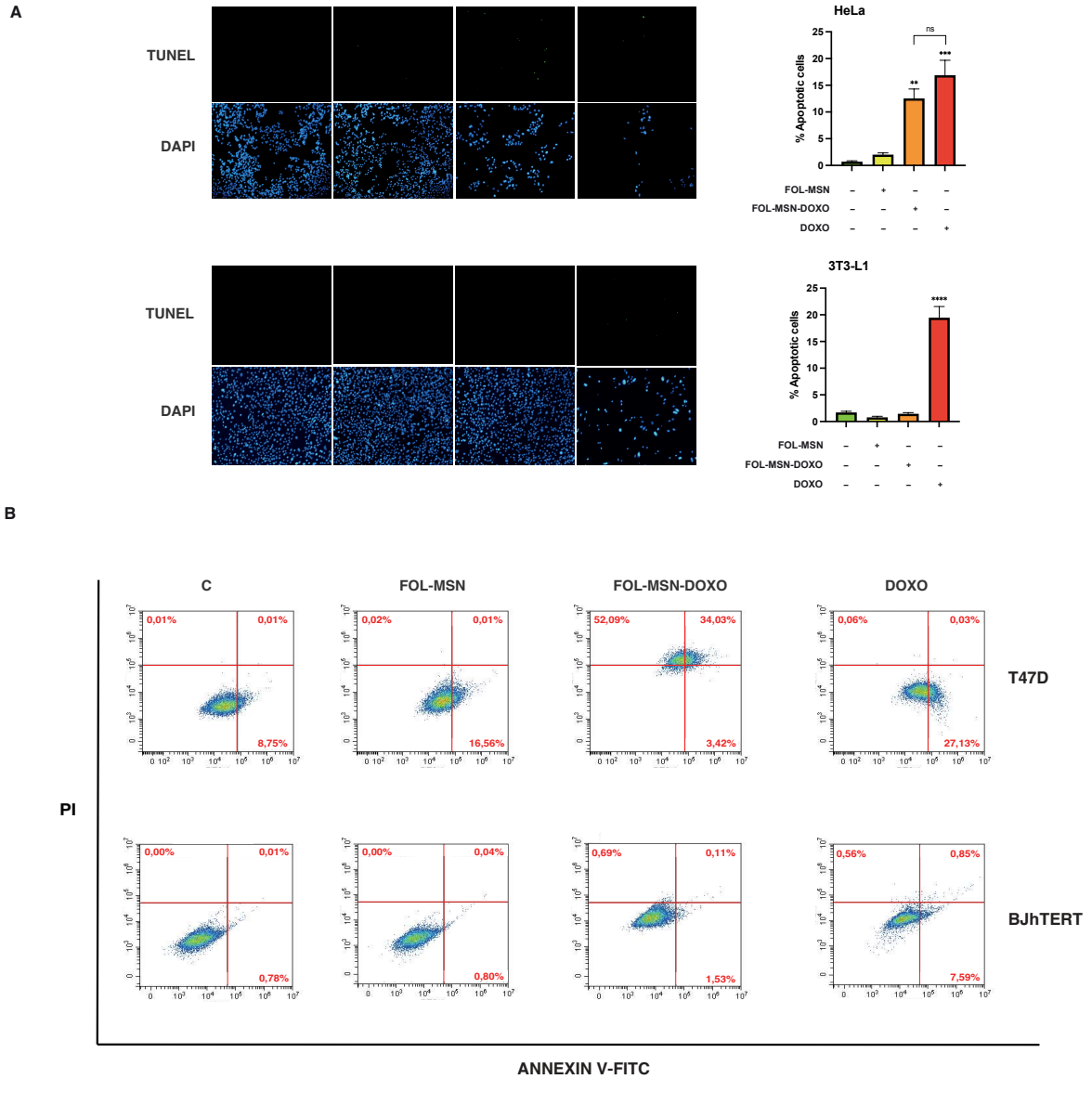

C

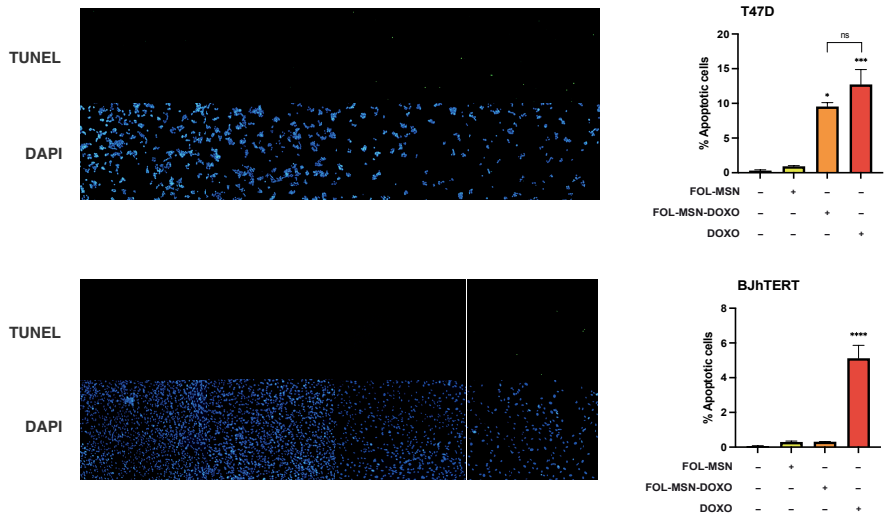

Figure 8. DOXO is not toxic to normal cells when bound to targeted MSNs. A) HeLa and 3T3-L1 were treated or not (control) with FOL-MSN, FOL-MSN-DOXO, and free DOXO for 1 hour. Cells were processed for TUNEL assay after 72 hours of treatment. Nuclei were counterstained with DAPI. Cells were photographed at 10× magnification, and apoptotic cells from triplicate experiments were counted using Image J software (graphs on the right). ** $p < 0.01$, *** $p \leq 0.001$ vs. control and FOL-MSN; **** $p \leq 0.0001$ vs. all other groups. **B**) T47D and BJhTERT cells were either treated with MSN-FOL, FOL-MSN-DOXO, and free DOXO or left untreated (control) for 1 hour, then stained with Annexin V-FITC and PI after 72 hours. Apoptosis was assessed by flow cytometry. The four quadrants represent living cells (lower left, Annexin V-/PI-), early apoptotic cells (lower right, Annexin V+/PI-), late apoptotic cells (upper right, Annexin V+/PI+), or necrotic cells (upper left, Annexin V-/PI+). Values represent the percentages of each quadrant. **C**) T47D and BJhTERT were treated as in (A) and processed for TUNEL assay after 72 hours of treatment. Cells were photographed at 10× magnification, and apoptotic cells from triplicate experiments were counted using Image J software (graphs on the right). * $p < 0.05$, p***<0.001 vs. control and FOL-MSN; **** $p \leq 0.0001$ vs. all other groups.

Notably, treatment with FOL-MSN alone produced no cytotoxic effect in either cell line, underlining the safety and biocompatibility of the mesoporous silica-based carrier. Overall, these results highlight the potential of the FOL-MSN-DOXO system to enhance the specificity of doxorubicin treatment by limiting damage to healthy cells while maintaining effective antitumor activity.

Several studies have demonstrated the potential of mesoporous silica nanoparticles (MSNs) functionalized with FOL for the pH-responsive, targeted delivery of doxorubicin (DOXO) to cancer cells. Most of these works, such as those by Cheng et al., Cao et al.,

Yang et al., and Beagan et al. [43-46] focused on the synthesis and in vitro evaluation of FOL-modified MSNs or related nanocarriers, showing enhanced drug release in acidic environments and selective cytotoxicity towards tumour cells, particularly in HepG2, MCF-7, or SMMC-7721 lines. However, these studies often lacked direct comparative analysis between cancerous and non-cancerous cells to assess targeting selectivity robustly.

In contrast, our work shows the effectiveness of FOL-functionalized MSNs in selectively delivering DOXO to tumor cells and provides clear evidence of biological selectivity through a systematic comparison between tumor and non-tumor cell lines. We demonstrated that our FOL-MSN-DOXO system significantly impaired cell proliferation, spheroid formation, and viability in cancer cells while preserving healthy cells' normal phenotype, survival, and apoptotic resistance. Molecular assays, including ROS generation, Annexin V/PI staining, TUNEL, and Western blotting for apoptotic markers, further corroborated this selective cytotoxicity.

In addition, doxorubicin can have neurotoxic effects, impacting the central (CNS) and peripheral nervous systems (PNS). In particular, doxorubicin has been implicated in cognitive impairment, occurring in 17% -75 % of cancer patients [47], highlighting the significant impact of this drug on neuronal function [13]. Beyond these effects, doxorubicin also significantly damages the peripheral nervous system, causing neuronal degeneration in the ganglia, as demonstrated in animal model studies [48-50]. The damage is mediated by oxidative stress, inflammation, and neuronal cell apoptosis, which compromise neuronal functionality [51].

These side effects not only limit the clinical use of doxorubicin but also highlight the urgency of developing effective therapeutic strategies to mitigate the neurotoxicity

associated with this drug, ultimately improving the quality of life for cancer patients. To achieve this goal, we tested our FOL-MSN-DOXO nanosystem using an ex vivo explant model of DRGs from neonatal rats, as described in Materials and Methods (**Fig. 9A**), aiming to replicate the physiological conditions of the PNS**.** DOXO treatment resulted in a significant decrease in the overall population of neurons, as shown by the reduction in the percentage of stained nuclei (**Fig. 9B**). In particular, Schwann cells (Sc), known for their crucial supportive and nutritional roles towards neurons [52, 53], exhibited a significant reduction in cell percentage and displayed marked morphological changes when exposed to free DOXO. The cells also became more aggregated and clustered, deviating from their typical spread-out arrangement (**Fig. 9B**, lower panel). This alteration may suggest a stress response or direct cytotoxicity that threatens the overall health of the neuronal microenvironment. Indeed, free DOXO also significantly reduced the number of neuronal cells, which lost their distinctive shape. The neurites appeared disorganized, fragmented, and, in some instances, abnormally retracted. These alterations suggest a disruption of the cytoskeletal framework, which is crucial for maintaining normal neuronal function [54] (**Fig. 9B**).

Conversely, when doxorubicin is administered via our MSNs, a slight, though not statistically significant, reduction in the number of nuclei is observed compared to control samples. Notably, the toxicity associated with FOL-MSN-DOXO is significantly lower. Both neurons and Schwann cells appear to be largely unaffected when compared to those treated with an equivalent dose of the free drug (**Fig. 9B**). Morphologically, both cell types retain their characteristic structure, exhibiting no apparent signs of degeneration or cellular distress. This reduced neurotoxicity can be attributed to a more controlled, pH-

sensitive release of doxorubicin. Our data show that FOL-MSN-DOXO releases the drug at pH 5, while the nervous system maintains a pH in a narrow range around 7.4 [55].

Notably, the overall pattern of neuronal cultures treated with FOL-MSN closely resembles that of the control group, indicating that the vehicle itself is nontoxic to neurons (**Fig. 9B**). This observation confirms results previously reported by our group [56], and it also aligns with previous studies highlighting the compatibility of mesoporous silica nanocarriers with the peripheral nervous system. Indeed, a mesoporous silica-based nanodevice bound to bisperoxovanadium (BpV), a PTEN inhibitor, has been successfully used in adult DRGs to stimulate the regenerative process in adult nervous tissues, promoting axonal growth [57].

FOL-MSN-DOXO nanoparticles were also tested on neuronal tumor cell lines, specifically the human SH-SY5Y cells and the murine neuroblastoma N2a cells. In contrast to the observations made in dorsal root ganglia (DRGs), treatment with FOL-MSN-DOXO significantly reduced the number of tumor cells at both concentrations tested (**Fig. 9C**). These results suggest that FOL-MSN-DOXO effectively induces a selective cytotoxic effect on neuron-derived tumor cells, while concurrently sparing normal neurons from the neurotoxic effects of doxorubicin. This underscores the potential of our nanosystem to strike a balance between therapeutic efficacy and neuronal safety.

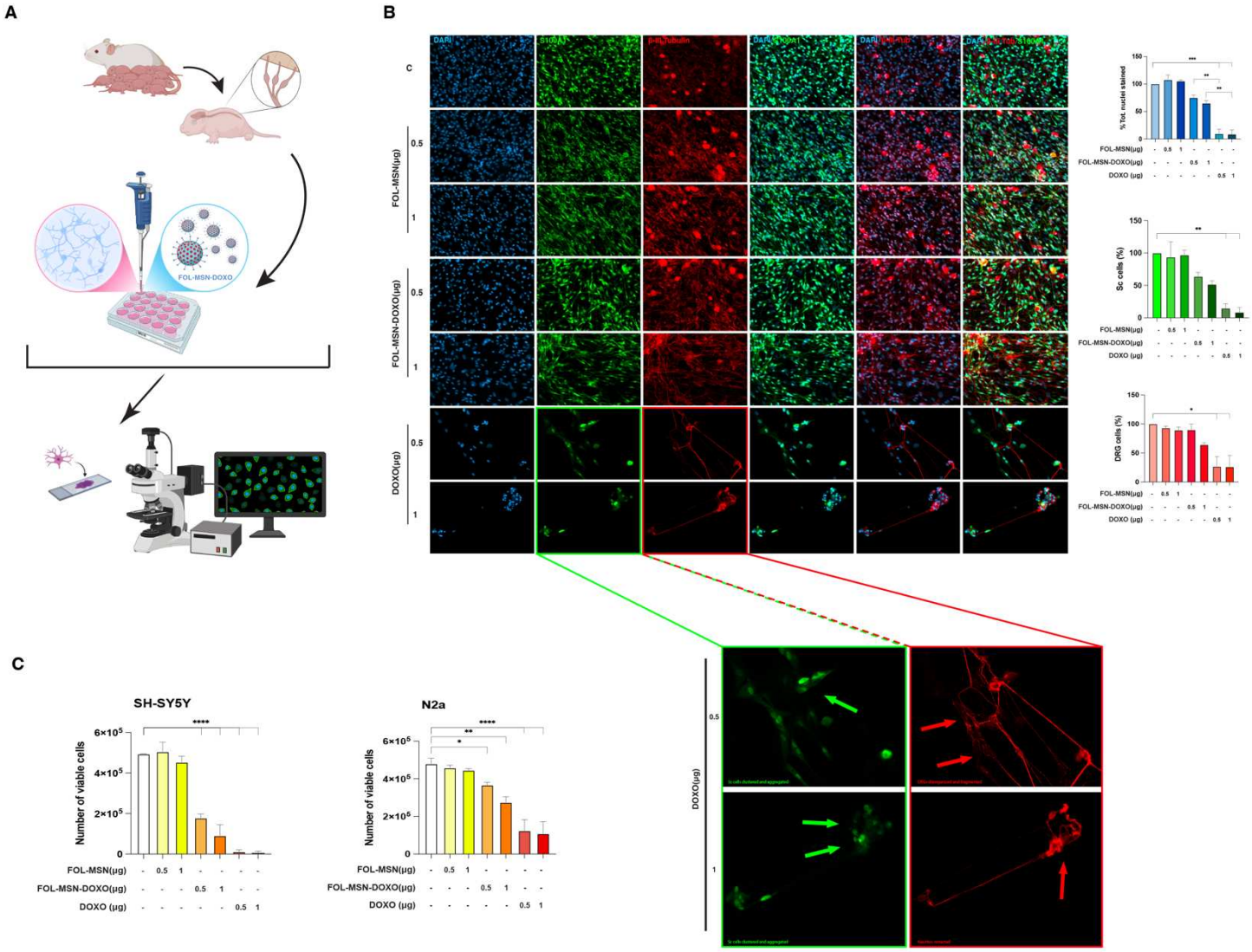

Figure 9. FOL-MSN-DOXO differently affects normal and tumoral neuronal cells

A) Experimental procedure for DRG extraction and treatment (see Materials and Methods for details). B) Representative images of immunofluorescence of primary DRG cultures stained with DAPI (blue), β-III-Tubulin (red) as a neuronal marker, and S100A1 (green) for Schwann cells (Sc). Cells were treated for 1 hour with 0.5 μg or 1 μg of FOL-MSN, FOL-MSN-DOXO, or free DOXO, or left untreated (Control), and then maintained in culture for 72 hours. Merged images of the individual channels are also provided. The graphs on the right show the percentage of total neuronal cells (stained nuclei), DRG neurons (β-III-tubulin+), and Schwann cells (S100A1+). Data are presented as mean ± SEM of three independent experiments (*p < 0.05, **p < 0.01, ***p < 0.001). Higher magnification images of DOXO-treated samples (bottom panel) reveal detailed morphological alterations in the architecture of Schwann and neuronal cells. C) Cytotoxic effect of FOL-MSN-DOXO on neuroblastoma cell lines SH-SY5Y and N2a. Cells were cultured as described for DRGs. After 72 hours, cell counting was performed using the Trypan Blue exclusion assay (*p < 0.05, **p < 0.01, ****p < 0.0001).

To our knowledge, this is the first study that uniquely examines the effect of mesoporous silica-based targeted chemotherapy on primary DRG cultures. Our findings demonstrate a preservation of neuronal viability, which is particularly noteworthy given the established neurotoxic profile linked to free doxorubicin. This protective effect is illustrated by the sustained neuronal morphology and integrity of cellular architecture in DRGs treated with FOL-MSN-DOXO, in stark contrast to the significant damage observed following treatment with free doxorubicin. While peripheral neuropathy affects a relatively small percentage of patients (approximately 12%) [58], our findings suggest that the FOL-MSN-DOXO nanosystem could offer an effective strategy to mitigate this adverse effect, thereby reducing its clinical impact. This research provides valuable insights into safer alternatives for chemotherapy that may help diminish neurotoxic effects.

Conclusion

In conclusion, our study demonstrates that the FOL-MSN-DOXO nanosystem, engineered with mesoporous silica nanoparticles functionalized on the exterior with folic acid and loaded with DOXO via a pH-sensitive linkage, thanks to the use of a hydrozone bond sensitive to the acidic environment, typical of the tumor microenvironment, provides an effective strategy for targeted cancer therapy.

Our data indicate that FOL-MSN-DOXO selectively mimics the cytotoxic efficacy of free doxorubicin in cancer cells without compromising the viability of healthy cells. Moreover, our *ex vivo* investigations using DRGs from neonatal rats also highlight the neuroprotective advantage of our approach. Unlike free doxorubicin, which causes significant neuronal damage and disrupts cellular architecture, treatment with FOL-MSN-DOXO preserves neuronal morphology and maintains the integrity of both neurons and Schwann cells. This reduced neurotoxicity is attributed to the controlled, pH-sensitive release of doxorubicin, which limits drug exposure to normal physiological environments. Overall, our findings not only underscore the enhanced anticancer efficacy of the FOL-MSN-DOXO system through its high selectivity for FR-positive tumor cells but also suggest that this nanosystem may mitigate doxorubicin-induced neurotoxicity. These results provide a strong foundation for further preclinical and clinical investigations, supporting the potential of FOL-MSN-DOXO as a safer and more effective therapeutic option for cancer treatment while minimizing adverse effects.

Bortezomib-loaded mesoporous silica nanoparticles selectively targets CD38-expressing multiple myeloma cells

Multiple myeloma (MM) is classified as a B-cell neoplasm characterized by the uncontrolled proliferation of malignant plasma cells, which secrete monoclonal immunoglobulins within the bone marrow (BM) [59]. According to the most recent estimates by GLOBOCAN 2022, MM accounts for approximately 188,000 new cases worldwide, with approximately 121,000 deaths attributable to the disease. The global age-standardized incidence (ASR) is 1.78 cases per 100,000 people, while in Europe, the incidence is around 6 cases per 100,000 inhabitants, and the median age at diagnosis is approximately 67 years [60].

This malignancy is further characterized by the widespread dissemination of tumor cells throughout the BM, which not only disrupts normal hematopoiesis but also contributes to skeletal complications. During MM progression, the normal equilibrium between osteoblastic (bone building) and osteoclastic (bone breakdown and resorption) activity is skewed toward net bone loss. MM-induced osteolysis releases growth factors embedded inside the bone matrix, fueling MM progression and expansion in the BM niche and resulting in greater osteoclastic activity in a process known as the “vicious cycle” [61]. The most widely used molecules include proteasome inhibitors, monoclonal antibodies, immunomodulatory agents (IMiDs), alkylators, and histone deacetylase inhibitors (DACIs).

Among the therapeutic approaches, bortezomib (BTZ) is the first proteasome inhibitor approved by the US FDA for the treatment of multiple myeloma patients [62, 63]. BTZ is a dipeptide boronic acid that reversibly inhibits the chymotrypsin-like activity (subunits

β5) of the 20S proteasome core in the 26S proteasome complex, consequently degrading cell proteins. The accumulation of proteins induces the overproduction of reactive oxygen species (ROS) in the ER, resulting in fatal cell stress and leading to cell cycle arrest and caspase-dependent apoptosis [64]. Therefore, ROS production and mitochondrial-mediated intracellular Ca2+ dysregulation [65] represent the main mechanisms of BTZ-induced cytotoxicity in MM cells.

Patients often discontinue BTZ treatment because of BTZ-induced peripheral neuropathy (BIPN) that occurs typically by the end of cycle 5 of chemotherapy treatment, with an estimated incidence of up to 40% of patients[65]. Peripheral neuropathy primarily manifests as sensory disturbances, with symptoms including burning sensations, paresthesia, hyperesthesia, hypoesthesia, neuropathic pain, and weakness. The specific mechanisms contributing to bortezomib-induced peripheral neuropathy (BIPN) remain poorly defined. Nevertheless, it is likely that a multifactorial etiology is involved, given the diverse array of sites affected by bortezomib-related damage, which includes the sensory cell bodies in the dorsal root ganglion (DRG) as well as the distal terminal axons. [64].

Cavaletti and colleagues, in their investigation utilizing a rat model to simulate the BiNP, posited that bortezomib (BTZ) induces a dying-back degeneration of sensory nerves, accompanied by pathological alterations in both Schwann cells and satellite cells. These findings are indicative of a toxic axonopathy [66]. In the same work, the authors also indicated that the DRG of BTZ-treated animals show intracytoplasmic vacuolization, which can be attributed to mitochondrial and endoplasmic reticulum enlargement [66, 67]. In addition, a subsequent investigation conducted by Meregalli and colleagues found that nerve terminals play a role in the development of BTZ neurotoxicity, resulting in

axonopathy of unmyelinated fibers, particularly affecting large and C-fiber damage [68]. In contrast, additional research indicated that BIPN primarily resulted from issues at the neuronal level, which subsequently affected the structures of axons and myelin [65]. Additionally, the inhibition of the proteasome by BTZ leads to the build-up of cytoplasmic aggregates in neuronal cells, a decrease in extranucleolar transcription, and the retention of polyadenylated RNAs within nuclear bodies in the nucleus [65].

Moreover, Alè et al. suggested that BTZ primarily impacted DRG neurons and caused dysfunction in neurite, affecting axonal transport, as sensory neurons are more susceptible to BTZ compared to Schwann cells [69]. Patients frequently report experiencing numbness or tingling in their hands and feet, along with burning pain, altered sensitivity to temperature and touch, muscle weakness, changes in the skin or nails, and/or difficulties with coordination. In fact, sensory neuropathy and neuropathic pain are commonly observed; as a result, terms such as hyperesthesia, hypoesthesia, and paraesthesia are often referenced, typically presenting in a distal stocking-and-glove distribution across the hands and feet, frequently accompanied by altered sensations of heat and cold. Additionally, sensory peripheral neuropathy can lead to areflexia and a reduced sense of proprioception. Symptoms or signs indicating damage to the motor and/or autonomic nervous systems may also manifest, though less frequently. Motor symptoms tend to arise in cases of severe sensory peripheral neuropathy, potentially resulting in muscle cramps, muscle atrophy, or diminished strength in the distal muscles. [65].

Furthermore, degeneration of axonal transport may occur as a result of a deficiency in mitochondrial energy metabolism and damage to the mitochondrial respiratory chain, which affects DRG neurons. Additionally, the neurotoxic effects of BTZ are attributed to

the temporary release of calcium from intracellular stores, which results in an influx of calcium into the mitochondria and apoptosis triggered by caspase activation. This was illustrated in a study by Landowski and colleagues involving myeloma cells treated with BTZ, where mitochondrial dysfunction led to reduced ATP levels [70].

In neurons, the disruption of calcium balance that causes depolarization and spontaneous firing is likely responsible for the characteristic degeneration seen in primary sensory neurons and intraepidermal nerve fibers in patients treated with BTZ [65]. Additionally, it is recognized that mitochondrial dysfunctions and oxidative stress—biochemical processes arising from the production of reactive oxygen species (ROS) in the electron transport chain—are present in BTZ-induced chronic painful peripheral neuropathy [70]. As a result, the production of oxidative stress could be a significant factor in the neuronal cell death caused by BTZ.

Given these challenges, the engineering of nanotechnology-based drug delivery systems (DDS) has received significant attention in the past two decades, owing to the potential that biocompatible nanomaterials can theoretically act as “magic bullets” and selectively deliver therapeutic agents to cancer cells while sparing normal tissues. The ultimate goal is to enable more effective treatment regimens by reducing drug concentration and dosing frequency, thus offering easier administrations and improving safety [71, 72].

Many conventional organic-based DDS (liposomes, micelles, dendrimers, and polymers) have reached the latest stages of development, but only a few have received FDA approval since their intrinsic instability and low drug-loading capacity/efficiency inhibit their further clinical translation [71, 73, 74].

Consequently, there has been growing interest in developing newer inorganic or organic/inorganic hybrid systems, with mesoporous silica nanoparticles (MSNs) emerging as promising candidates. MSNs present a robust framework characterized by uniformly sized pores ranging from 15 to 100 Å, enabling the encapsulation of both hydrophobic and hydrophilic therapeutic agents, as well as providing a high surface area capable of hosting targeting groups. These attributes bestow MSNs with a unique advantage for the direct delivery of therapeutic and diagnostic (theranostic) agents—such as drugs, siRNA, miRNA, enzymes, proteins, DNA, and imaging probes—to specific locations, such as tumors [73, 75-77].

The functionalization of the silica surface with stimuli-responsive molecules—ranging from macrocyclic compounds to linear molecules, polymers, proteins, and magnetic nanoparticles, typically referred to as capping, gating, or gatekeeper agents—affords precise control over drug release by preventing premature leakage until specific environmental conditions, such as pH changes, are met [78]. In this context, the development of pH-sensitive systems has been extensively pursued in cancer therapy, given that neoplastic cells display a more acidic microenvironment relative to normal cells, with endosomes and lysosomes exhibiting pH values of 4.5–5.5. Upon cellular internalization of these pH-sensitive MSNs, the lower pH within lysosomes triggers drug release, thereby achieving the desired therapeutic efficacy.

Despite significant progress in the management of MM over the past 20 years, a definitive cure remains elusive, and there is an ongoing need for novel therapeutic strategies that not only extend patient survival but also enhance quality of life. In this context, the highly innovative multifunctional MSN technology represents a potential drug delivery platform for the treatment of multiple myeloma. Traditionally, MSNs have been functionalized on

the external surface with various targeting ligands, such as folic acid, via amide bond formation, while their inner pore surfaces are used to host drugs like BTZ through pH-sensitive bonds. The as-synthetized materials were functionalized on the external surface with the targeting ligand CD38 by amide bond formation, and the inner pore surface hosts the drug BTZ through a pH-sensitive bond.

A particularly noteworthy advancement is the incorporation of CD38 as the external targeting ligand. CD38, a type II transmembrane glycoprotein, was discovered in 1980 by E.L. Reinherz and S. Schlossman [79]. It regulates migration, receptor-mediated adhesion by interaction with CD31 or hyaluronic acid, and signaling events [80]. Furthermore, CD38 also has ectoenzymatic activity and is involved in the generation of nucleotide metabolites, which play a role in controlling intracellular calcium stores [79]. Under normal conditions, CD38 is expressed at relatively low levels on myeloid and lymphoid cells and in some non-hematopoietic tissues [81, 82]. In contrast, plasma cells and multiple myeloma cells have high levels of CD38 expression, which makes CD38 an interesting target for therapeutic antibodies targeting cell surface molecules in MM [83].

Daratumumab (fully human; Janssen Pharmaceuticals) is the first CD38-targeting antibody, which is approved as a single agent and in combination with several standards of care in MM [83]. CD38 antibodies are evaluated in relapsed/refractory MM but also in patients with newly diagnosed MM [79]

CD38 antibodies kill tumor cells via Fc-dependent immune effector mechanisms, including complement-dependent cytotoxicity (CDC), antibody-dependent cell-mediated cytotoxicity (ADCC), antibody-dependent cellular phagocytosis (ADCP), and apoptosis upon secondary cross-linking [80].

In this work, we have synthesized a novel drug delivery system comprising mesoporous silica nanoparticles (MSNs) loaded with bortezomib (BTZ) and functionalized on the external surface with CD38 as the targeting moiety (Fig.8). This innovation represents a significant advancement over previous MSN-based systems that employed folic acid as the targeting ligand[35, 84]. By substituting folic acid with CD38, our approach leverages the high expression of CD38 on MM cells to ensure the selective delivery of BTZ directly to the tumor site. The nanoparticles were synthesized by encapsulating BTZ within the MSN pores through a pH-sensitive bond, while CD38-targeting ligands were conjugated to the external surface via amide bond formation. This configuration facilitates targeted binding to MM cells and minimizes off-target toxicity.

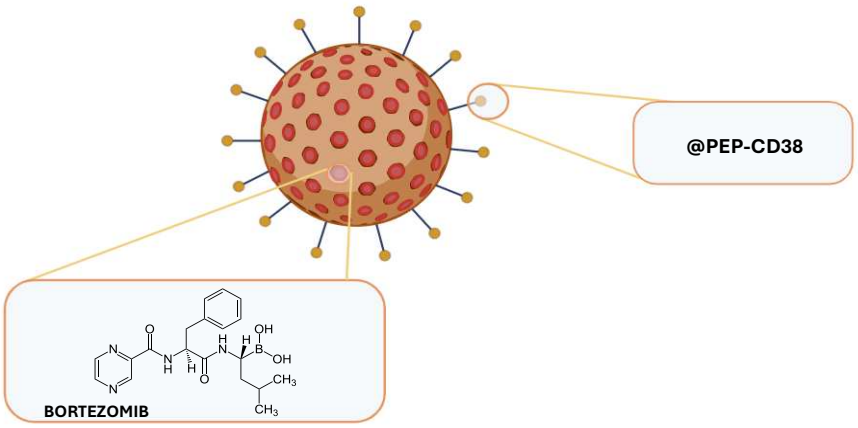

Figure 8. Structural Representation of the CD38-MSN-BTZ Nanosystem

To evaluate the efficacy and specificity of the CD38-MSN-BTZ system, in vitro studies were conducted using RPMI 8226 MM cell lines alongside normal cells. Proliferation assays were employed to assess the impact of the nanoparticles on cell viability. At the same time, transmission electron microscopy (TEM) was utilized to confirm the drug-

loaded nanoparticles' internalization and analyze their intracellular distribution. Moreover, immunofluorescence staining on dorsal root ganglion (DRG) neurons was performed to investigate the potential neurotoxic effects of the CD38-targeted system.

In summary, this integrated approach not only underscores the potential of nanotechnology in enhancing drug delivery for multiple myeloma but also highlights the innovative use of CD38 as a targeting ligand to improve specificity. The CD38-MSN-BTZ system represents a promising advancement aimed at reducing systemic toxicity and enhancing therapeutic outcomes in MM patients. Continued evaluation of this novel platform may pave the way for more precise and effective treatments in the fight against multiple myeloma.

MATERIALS AND METHODS

6.1 Chemicals and reagents.

Dulbecco's Modified Eagle's Medium (DMEM), RPMI 1640 (1x) Medium, Dulbecco's Modified Eagle Medium/Nutrient Mixture F-12 (DMEM/F-12), L-Glutamine, penicillin/streptomycin (pen/strep), Fetal Bovine Serum (FBS) and phosphate-buffered saline (PBS) were from Gibco™ (Life Technologies, Monza MB, Italy). Trypsin-EDTA solution 10x, protease inhibitors (cOmplete™ ULTRA Tablets, cat#5892970001), and Bortezomib by MERCK/Sigma-Aldrich (Milan, Italy). Bortezomib was dissolved, for all the treatments, in ethanol at the final concentration 1mg/ml.

6.2 Cell cultures and treatments.

Human MM RPMI-8226 (RPMI) and human neuroblastoma SH-SY5Y were purchased from ATCC, where they were authenticated. Cells were stored in accordance with the supplier's specifications and were utilized within six months following the resuscitation of frozen aliquots. Normal foreskin fibroblast BJhTERT cells were kindly provided by Michael Lisanti, University of Salford, Manchester (UK). Cells were purchased from ATCC, transferred to our laboratory at passage n=3, and handled as described above. RPMI were cultured in RPMI-1640 medium, BJhTERT in DMEM, and SH-SY5Y were maintained in DMEM high-glucose supplemented with 10% FBS, 100IU ml-1 pen/strep, and 0,2 mM L-Glutamine. Mycoplasma testing was conducted monthly using PlasmoTest from Invivogen, Aurogene, Rome IT. A treatment ratio of 1 μg MSNs per 10^5 cells was determined based on titration experiments. Free BTZ was included as a positive control at levels that matched the percentage of BTZ present in CD38-MSN-BTZ.

6.2.1 Western Blotting (WB) Assay

Total protein extracts were prepared by lysing the cells with RIPA buffer (Sigma Aldrich) supplemented with a protease inhibitor cocktail (aprotinin, phenylmethylsulfonyl fluoride, and sodium orthovanadate). The protein content was determined using Bradford dye reagent (Bio-Rad, Milan, Italy). 30 μg of denatured proteins were run on a 10% polyacrylamide gel and transferred to nitrocellulose membranes. Proteins were detected using Anti-CD38 [EPR4106] ab108403 (Abcam) anti-β-Actin (AC-15, A1978)

The proteins were detected with specific polyclonal (p) or monoclonal (m) antibodies (Abs), recognized by IRDye secondary Abs (LI-COR Corporate, Nebraska, USA). Images were acquired with the Odyssey FC Imaging System (LI-COR Corporate).

6.2.2 Cell proliferation assays.

The effect of MSNs on cell proliferation was assessed using a trypan blue exclusion assay. Cells were plated in triplicate for each condition, synchronized in serum-free media (SFM) for 24 hours, and then treated with MSNs at a concentration of 1 μg per 10^5 cells for 1 hour. Following treatment, the cells were transferred to fresh growth medium supplemented with 1% FBS and counted after 72 hours. Cell viability was determined using the Countess method.

6.2.3 Transmission electron microscopy (TEM) and electron immunocytochemistry

For conventional TEM analysis, cells were seeded at a density of approximately 1×10^6 per 60-mm plate and treated as for the proliferation assay. All samples were routinely fixed, dehydrated, and resin-embedded using heat polymerization as previously described

[35]. For indirect immunolabeling, grids were floated on 1% bovine serum albumin (BSA) drops in PBS containing 0.02 M glycine at room temperature for 30 minutes to minimize nonspecific binding. The sections were then incubated overnight with a mouse monoclonal antibody against Anti-CD38 [EPR4106] ab108403 (Abcam) at 277.15 K. Subsequently, the grids were transferred to 50 µL drops of a secondary antibody conjugated to 10 nm gold particles, where they were incubated for 1 hour at room temperature. Observations were conducted using a Jeol JEM-1400 Plus electron microscope (Jeol Ltd, Tokyo, Japan) operating at 80 kV.

6.2.4 Culture of dissociated DRGs, treatment, and immunofluorescence

Dorsal root ganglia (DRGs), the primary neurons in the sensory pathway, were isolated from neonatal Sprague Dawley rats on postnatal days 3–4 (P3–P4). Briefly, DRGs were dissected from all spinal segments, pooled, and collected in cold Hank's Balanced Salt Solution (HBSS). Residual spinal roots and attached nerves were carefully removed. DRGs were then enzymatically digested with collagenase IA (Sigma, cat. no. C9891) for 35 minutes, followed by 7-minute digestion with TrypLE (Gibco). After digestion, DRGs were resuspended in a complete culture medium (MM: DMEM/F12 supplemented with 10% fetal bovine serum [FBS], 1% penicillin/streptomycin [P/S], and 2.5 ng/µL nerve growth factor [NGF, Gibco). The cells were then mechanically dissociated using a 1,000 µL blue pipette tip and plated onto coverslips pre-coated overnight at 37°C with poly-L-lysine (Sigma, 20 µg/mL), followed by laminin (Sigma, 10 µg/mL) for 3 hours at 37°C. Cells were seeded at a density of 100,000 cells per well in a 24-well plate and treated with either vehicle alone (CD38-MSN) or drug-loaded nanoparticles (CD38-MSN-BTZ) at doses equivalent to two different concentrations of free BTZ (0.5 µg, 1 µg and 2 µg

/100,000 cells), which served as positive controls. One hour after treatment, the culture medium was replaced with fresh MM medium. After 72 hours, coverslips were fixed in 4% paraformaldehyde for 10 minutes, followed by blocking with 3% normal goat serum (NGS) for 1 hour at room temperature. Subsequently, coverslips were incubated overnight in a humid chamber with a rabbit anti-S100A1 (Z0311, DAKO) and a mouse anti-β-III-Tubulin (AB7751, Abcam) primary antibodies, S100A1 being a marker for Schwann cells (Sc) and β-III-Tubulin a neuronal marker. Alexa Fluor 488-(A21202, Invitrogen) and 647-(A31573, Invitrogen) conjugated secondary antibodies were used for the respective primaries and incubated for 1 hour at room temperature. Finally, coverslips were counterstained with DAPI (D9542, Sigma) and mounted with Mowiol (81381, Sigma). Images were acquired from Leica DMI8 inverted and analyzed using ImageJ.

In vitro evaluation of CD38-MSN-BTZ nanosystem

7.1 Results and Discussion

To assess the selectivity of the CD38-MSN-BTZ nanovehicle for CD38-expressing cells, RPMI cells were employed as a model for CD38-positive tumor cells, while BJhTERT cells served as a model for CD38-negative normal cells. This choice was validated by Western blot analysis (**Fig. 1A**), which showed a significantly higher expression of CD38 in multiple myeloma cells compared to normal cells. Subsequent proliferation assays in the RPMI cell line revealed that CD38-MSN-BTZ effectively induces cell death in these tumor cells, exhibiting an efficacy comparable to that of the free drug; conversely, the BJhTERT cell line only responded to treatment with BTZ alone (**Fig. 1B**).

Furthermore, immunogold labeling experiments on RPMI cells confirmed that the recognition and uptake of the CD38-MSN nano vehicle are dependent on CD38. As demonstrated in **Fig. 1C**, two representative images depict the CD38-mediated endocytic pathway—from receptor recognition at the cell membrane to internalization into CD38-immunopositive intracellular vesicles.

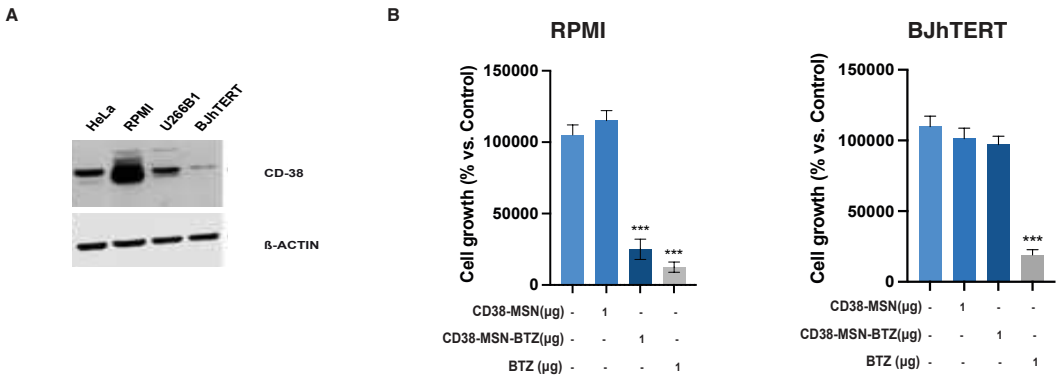

c

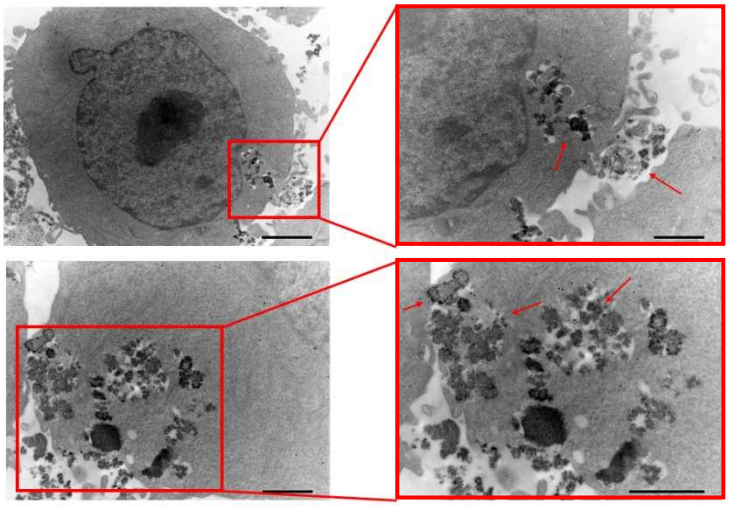

Figure 1: A) Protein expression of CD38 in different cell lines. 30µg of denatured proteins from total lysates were loaded and subjected to WB analysis. β-actin was used as a loading control. **B**) Normal BJhTERT cells and cancerous CD38+ RPMI cells were left untreated or treated for 1h with CD38-MSN, CD38-MSN-BTZ, or free BTZ. Viability was determined after 3 days. Representative images of three independent experiments are shown. *** $p \leq 0.001$ vs control.

Bortezomib has been widely associated with the onset of chemotherapy-induced peripheral neuropathy (CIPN), with clinical studies indicating an incidence rate ranging from 31% to 37%, and grade ≥2 neuropathy occurring in approximately 28% of treated patients [85, 86]. The resulting condition, known as bortezomib-induced peripheral neuropathy (BIPN), typically presents as a distal, symmetric, length-dependent axonal neuropathy that affects both sensory and motor functions. It is commonly characterized by mild to moderate sensory deficits, neuropathic pain of varying intensity, and mild motor weakness, particularly affecting the distal regions of the lower limbs [87]. To assess whether our MSN-based delivery system can mitigate bortezomib's neurotoxic effects, we conducted experiments using an ex vivo explant model of dorsal root ganglia (DRGs) isolated from neonatal rats to mimic the physiological environment of the peripheral

nervous system (PNS). Treatment with free BTZ resulted in a marked reduction in the neuronal population, as indicated by a decreased percentage of stained nuclei (**Fig. 2A**). In particular, Schwann cells—essential for neuronal support and nutrition— showed a significant decrease in cell number following exposure to the free drug. In contrast, administration of bortezomib via our MSNs did not reduce nuclei count relative to control samples, with no observable toxicity at any of the tested doses of CD38-MSN-BTZ.

Both neurons and Schwann cells retained their viability, and the cultures treated with CD38-MSN displayed a profile nearly identical to the untreated controls, confirming the safety of the delivery vehicle (**Fig. 2A**). Moreover, when assessed in a neuron-derived tumor model using human SH-SY5Y cells, CD38-MSN-BTZ treatment significantly reduced tumor cell numbers at concentrations of 1 μg and 2 μg (**Fig. 2B**). These results demonstrate that CD38-MSN-BTZ selectively targets neuronal tumor cells while preserving the integrity and viability of normal peripheral neurons, offering a promising strategy to minimize bortezomib-induced neurotoxicity.

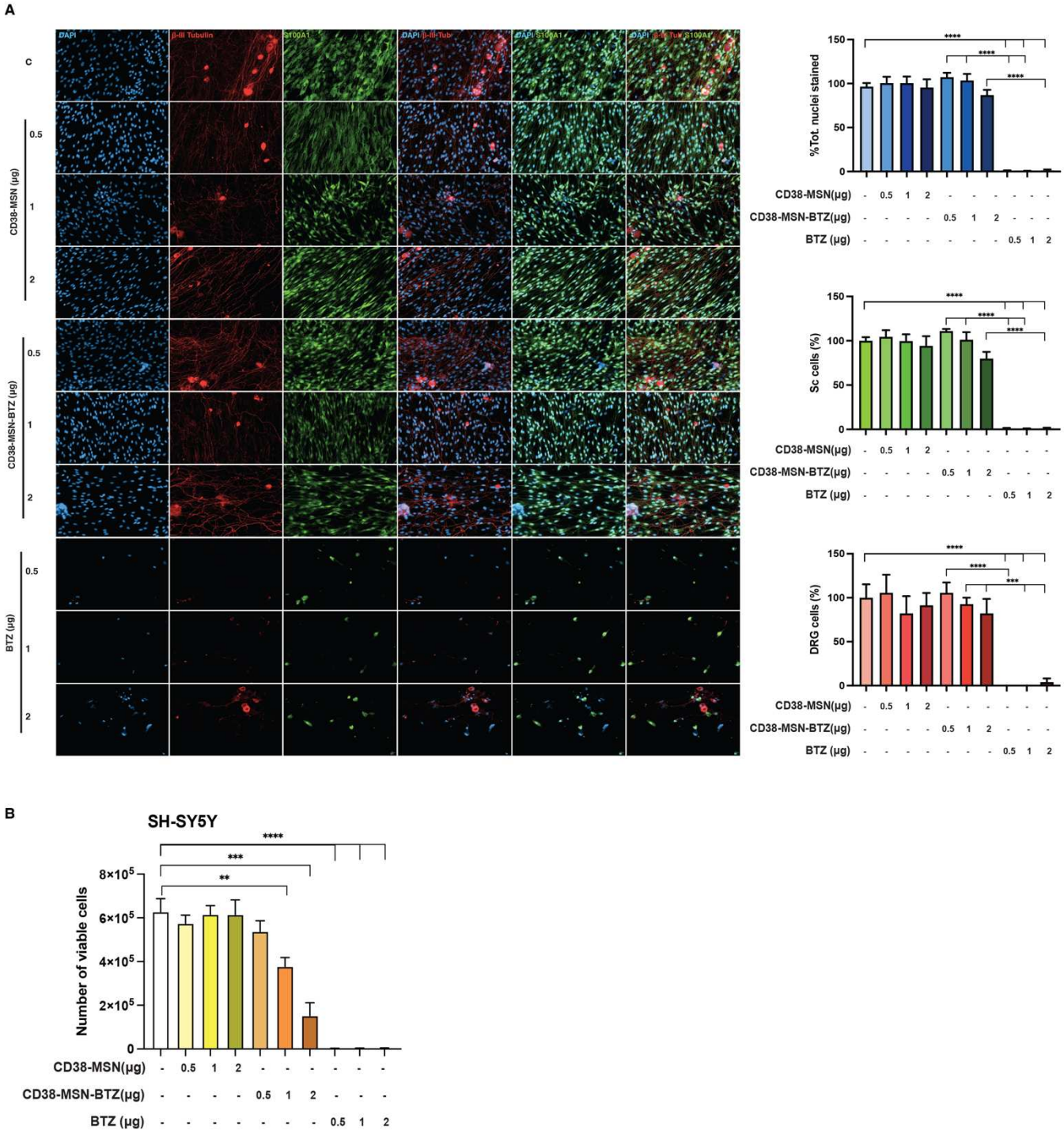

Figure 2. CD38-MSN-BTZ differently affects normal and tumoral neuronal cells

A) Representative images of immunofluorescence of primary DRG cultures stained with DAPI (blue), β-III-Tubulin (red) as a neuronal marker, and S100A1 (green) for Schwann cells (Sc). Cells were treated for 1 hour with 0.5 μg, 1 μg, and 2 μg of CD38-MSN, CD38-MSN-BTZ, or free BTZ, or left untreated (Control), and then maintained in culture for 72 hours. Merged images of the individual channels are also provided. The graphs on the right show the percentage of total neuronal cells (stained nuclei), DRG neurons (β-III-tubulin+), and Schwann cells (S100A1+). Data are presented as mean ± SEM of three independent experiments (****p < 0.0001, ***p < 0.001). **B**) Cytotoxic effect of CD38-MSN-BTZ on neuroblastoma cell line SH-SY5Y. Cells were cultured as described for DRGs. After 72 hours, cell counting was performed using the Trypan Blue exclusion assay (**p < 0.01, ***p < 0.001, ****p < 0.0001).

Importantly, primary DRG cultures treated with CD38-MSN-BTZ nanoparticles exhibited no detectable neurotoxicity, with cell viability and morphology remaining comparable to untreated controls. In contrast, free bortezomib induced significant cytotoxic effects across all tested doses, leading to widespread neuronal and glial damage. These results strongly indicate that encapsulating bortezomib within our pH-sensitive, CD38-targeted mesoporous silica nanoparticles dramatically mitigates the drug's neurotoxic effects, suggesting a promising neuroprotective advantage. Notably, this study is the first to report a mesoporous silica-based nanovehicle designed for selective delivery of bortezomib via CD38 targeting, filling a critical gap in the literature. While these *ex vivo* findings are highly encouraging, further *in vivo* studies are essential to validate the translational potential of our approach for reducing bortezomib-induced neuropathy in clinical settings.

References

1. Ferlay J, E.M., Lam F, Laversanne M, Colombet M, Mery L, Piñeros M, Znaor A, Soerjomataram I, Bray F *Global Cancer Observatory: Cancer Today. Lyon, France: International Agency for Research on Cancer.* . 2024; Available from: https://gco.iarc.who.int/media/globocan/factsheets/cancers/20-breast-fact-sheet.pdf, https://gco.iarc.who.int/media/globocan/factsheets/cancers/23-cervix-uteri-fact-sheet.pdf
2. Kciuk, M., et al., *Doxorubicin-An Agent with Multiple Mechanisms of Anticancer Activity.* Cells, 2023. **12**(4).
3. Arcamone, F., et al., *Adriamycin, 14-hydroxydaunomycin, a new antitumor antibiotic from S. peucetius var. caesius.* Biotechnol Bioeng, 1969. **11**(6): p. 1101-10.
4. Denel-Bobrowska, M. and A. Marczak, *Structural modifications in the sugar moiety as a key to improving the anticancer effectiveness of doxorubicin.* Life Sci, 2017. **178**: p. 1-8.
5. Pérez-Arnaiz, C., et al., *New insights into the mechanism of the DNA/doxorubicin interaction.* J Phys Chem B, 2014. **118**(5): p. 1288-95.
6. Gorini, S., et al., *Chemotherapeutic Drugs and Mitochondrial Dysfunction: Focus on Doxorubicin, Trastuzumab, and Sunitinib.* Oxid Med Cell Longev, 2018. **2018**: p. 7582730.
7. Christidi, E. and L.R. Brunham, *Regulated cell death pathways in doxorubicin-induced cardiotoxicity.* Cell Death Dis, 2021. **12**(4): p. 339.
8. Li, Y., J. Yan, and P. Yang, *The mechanism and therapeutic strategies in doxorubicin-induced cardiotoxicity: Role of programmed cell death.* Cell Stress Chaperones, 2024. **29**(5): p. 666-680.
9. Chatterjee, K., et al., *Doxorubicin cardiomyopathy.* Cardiology, 2010. **115**(2): p. 155-62.
10. Injac, R. and B. Strukelj, *Recent advances in protection against doxorubicin-induced toxicity.* Technol Cancer Res Treat, 2008. **7**(6): p. 497-516.
11. Chen, T., et al., *A herbal formula, SYKT, reverses doxorubicin-induced myelosuppression and cardiotoxicity by inhibiting ROS-mediated apoptosis.* Mol Med Rep, 2017. **15**(4): p. 2057-2066.
12. Alhowail, A.H., et al., *Doxorubicin-induced neurotoxicity is associated with acute alterations in synaptic plasticity, apoptosis, and lipid peroxidation.* Toxicol Mech Methods, 2019. **29**(6): p. 457-466.
13. Kamińska, K. and A. Cudnoch-Jędrzejewska, *A Review on the Neurotoxic Effects of Doxorubicin.* Neurotox Res, 2023. **41**(5): p. 383-397.
14. Curigliano, G., et al., *Cardiotoxicity of anticancer treatments: Epidemiology, detection, and management.* CA Cancer J Clin, 2016. **66**(4): p. 309-25.
15. Cardinale, D., G. Biasillo, and C.M. Cipolla, *Curing Cancer, Saving the Heart: A Challenge That Cardioncology Should Not Miss.* Curr Cardiol Rep, 2016. **18**(6): p. 51.
16. Bloom, M.W., et al., *Cancer Therapy-Related Cardiac Dysfunction and Heart Failure: Part 1: Definitions, Pathophysiology, Risk Factors, and Imaging.* Circ Heart Fail, 2016. **9**(1): p. e002661.
17. Nitiss, K.C. and J.L. Nitiss, *Twisting and ironing: doxorubicin cardiotoxicity by mitochondrial DNA damage.* Clin Cancer Res, 2014. **20**(18): p. 4737-9.
18. Zamorano, J.L., et al., *2016 ESC Position Paper on cancer treatments and cardiovascular toxicity developed under the auspices of the ESC Committee for Practice Guidelines: The Task Force for cancer treatments and cardiovascular toxicity of the European Society of Cardiology (ESC).* Eur Heart J, 2016. **37**(36): p. 2768-2801.
19. Shams, F., et al., *Nanotechnology-based products for cancer immunotherapy.* Mol Biol Rep, 2022. **49**(2): p. 1389-1412.
20. Wakaskar, R.R., *Promising effects of nanomedicine in cancer drug delivery.* J Drug Target, 2018. **26**(4): p. 319-324.

21. Barenholz, Y., *Doxil®--the first FDA-approved nano-drug: lessons learned.* J Control Release, 2012. **160**(2): p. 117-34.
22. Gan, Y., et al., *Liposomal Nanomaterials: A Rising Star in Glioma Treatment.* Int J Nanomedicine, 2024. **19**: p. 6757-6776.
23. Yingchoncharoen, P., D.S. Kalinowski, and D.R. Richardson, *Lipid-Based Drug Delivery Systems in Cancer Therapy: What Is Available and What Is Yet to Come.* Pharmacol Rev, 2016. **68**(3): p. 701-87.
24. Tang, F., L. Li, and D. Chen, *Mesoporous silica nanoparticles: synthesis, biocompatibility and drug delivery.* Adv Mater, 2012. **24**(12): p. 1504-34.
25. Xu, B., et al., *Multifunctional mesoporous silica nanoparticles for biomedical applications.* Signal Transduction and Targeted Therapy, 2023. **8**(1): p. 435.
26. Castillo, R.R., et al., *Advances in mesoporous silica nanoparticles for targeted stimuli-responsive drug delivery: an update.* Expert Opin Drug Deliv, 2019. **16**(4): p. 415-439.
27. Mohammadpour, R., et al., *One-year chronic toxicity evaluation of single dose intravenously administered silica nanoparticles in mice and their Ex vivo human hemocompatibility.* J Control Release, 2020. **324**: p. 471-481.
28. Kang, Y., et al., *Oligo Hyaluronan-Coated Silica/Hydroxyapatite Degradable Nanoparticles for Targeted Cancer Treatment.* Adv Sci (Weinh), 2019. **6**(13): p. 1900716.
29. Mal, A., et al., *pH-responsive sustained delivery of doxorubicin using aminated and PEGylated mesoporous silica nanoparticles leads to enhanced antitumor efficacy in pre-clinical orthotopic breast cancer model.* Journal of Drug Delivery Science and Technology, 2022. **77**: p. 103800.
30. Li, M., et al., *Structural basis of dual Ca(2+)/pH regulation of the endolysosomal TRPML1 channel.* Nat Struct Mol Biol, 2017. **24**(3): p. 205-213.
31. Hosonuma, M. and K. Yoshimura, *Association between pH regulation of the tumor microenvironment and immunological state.* Front Oncol, 2023. **13**: p. 1175563.
32. Czupiel, P., V. Delplace, and M. Shoichet, *Nanoparticle delivery of a pH-sensitive prodrug of doxorubicin and a mitochondrial targeting VES-H8R8 synergistically kill multi-drug resistant breast cancer cells.* Scientific Reports, 2020. **10**(1): p. 8726.
33. Etrych, T., et al., *HPMA copolymer conjugates of paclitaxel and docetaxel with pH-controlled drug release.* Mol Pharm, 2010. **7**(4): p. 1015-26.
34. Bae, Y., et al., *Design of Environment-Sensitive Supramolecular Assemblies for Intracellular Drug Delivery: Polymeric Micelles that are Responsive to Intracellular pH Change.* Angewandte Chemie International Edition, 2003. **42**(38): p. 4640-4643.
35. De Santo, M., et al., *Engineered mesoporous silica-based nanoparticles as smart chemotherapy nanodevice for bortezomib administration.* Materials Chemistry Frontiers, 2023. **7**(2): p. 216-229.
36. Lu, Y. and P.S. Low, *Folate-mediated delivery of macromolecular anticancer therapeutic agents.* Adv Drug Deliv Rev, 2002. **54**(5): p. 675-93.
37. Ebrahimnejad, P., et al., *An updated review of folate-functionalized nanocarriers: A promising ligand in cancer.* Drug Discovery Today, 2022. **27**(2): p. 471-489.
38. Hussain, A., et al., *Application of curcumin nanoformulations to target folic acid receptor in cancer: Recent trends and advances.* Environmental Research, 2023. **233**: p. 116476.
39. Augustine, R., et al., *Cellular uptake and retention of nanoparticles: Insights on particle properties and interaction with cellular components.* Materials Today Communications, 2020. **25**: p. 101692.
40. Morelli, C., et al., *PEG-templated mesoporous silica nanoparticles exclusively target cancer cells.* Nanoscale, 2011. **3**(8): p. 3198-3207.
41. Pietkiewicz, S., J.H. Schmidt, and I.N. Lavrik, *Quantification of apoptosis and necroptosis at the single cell level by a combination of Imaging Flow Cytometry with classical Annexin V/propidium iodide staining.* Journal of Immunological Methods, 2015. **423**: p. 99-103.

42. Eidet, J.R., et al., *Objective assessment of changes in nuclear morphology and cell distribution following induction of apoptosis.* Diagn Pathol, 2014. **9**: p. 92.
43. Cheng, W., et al., *pH-Sensitive Delivery Vehicle Based on Folic Acid-Conjugated Polydopamine-Modified Mesoporous Silica Nanoparticles for Targeted Cancer Therapy.* ACS Appl Mater Interfaces, 2017. **9**(22): p. 18462-18473.
44. Beagan, A.M., et al., *Folic Acid-Terminated Poly(2-Diethyl Amino Ethyl Methacrylate) Brush-Gated Magnetic Mesoporous Nanoparticles as a Smart Drug Delivery System.* Polymers (Basel), 2020. **13**(1).
45. Cao, Y., et al., *Folate functionalized pH-sensitive photothermal therapy traceable hollow mesoporous silica nanoparticles as a targeted drug carrier to improve the antitumor effect of doxorubicin in the hepatoma cell line SMMC-7721.* Drug Deliv, 2020. **27**(1): p. 258-268.
46. Yang, K., et al., *Intracellular pH-Triggered, Targeted Drug Delivery to Cancer Cells by Multifunctional Envelope-Type Mesoporous Silica Nanocontainers.* ACS Appl Mater Interfaces, 2015. **7**(31): p. 17399-407.
47. El-Agamy, S.E., et al., *Chemotherapy and cognition: comprehensive review on doxorubicin-induced chemobrain.* Cancer Chemotherapy and Pharmacology, 2019. **84**(1): p. 1-14.
48. E. S. Cho, P.S.S., B. S. Jortner, H. H. Schaumburg, *A single intravenous injection of doxorubicin (Adriamycin®) induces sensory neuronopathy in rats.* NeuroToxicology, 1980. **Vol. 1, No. 3.**: p. pp. 583-591.
49. Cho, E.-S., *Toxic Effects of Adriamycin on the Ganglia of the Peripherial Nervous System: A Neuropathological Study.* Journal of Neuropathology & Experimental Neurology, 1977. **36**(6): p. 907-915.
50. Kondo, A., et al., *Neurotoxicity in primary sensory neurons of adriamycin administered through retrograde axoplasmic transport in rats.* Neuropathol Appl Neurobiol, 1987. **13**(3): p. 177-92.
51. Alhowail, A.H., et al., *Doxorubicin-induced neurotoxicity is associated with acute alterations in synaptic plasticity, apoptosis, and lipid peroxidation.* Toxicology Mechanisms and Methods, 2019. **29**(6): p. 457-466.
52. Bunge, R.P., *The role of the Schwann cell in trophic support and regeneration.* J Neurol, 1994. **242**(1 Suppl 1): p. S19-21.
53. Jessen, K.R. and R. Mirsky, *The origin and development of glial cells in peripheral nerves.* Nat Rev Neurosci, 2005. **6**(9): p. 671-82.
54. Dimitrakis, P., et al., *Effects of doxorubicin cancer therapy on autophagy and the ubiquitin-proteasome system in long-term cultured adult rat cardiomyocytes.* Cell Tissue Res, 2012. **350**(2): p. 361-72.
55. Jalalvand, E., et al., *The Spinal Cord Has an Intrinsic System for the Control of pH.* Current Biology, 2016. **26**(10): p. 1346-1351.
56. Ceresa, C., et al., *Functionalized mesoporous silica nanoparticles: a possible strategy to target cancer cells reducing peripheral nervous system uptake.* Curr Med Chem, 2013. **20**(20): p. 2589-600.
57. Kim, M.S., et al., *Nanotherapeutics of PTEN Inhibitor with Mesoporous Silica Nanocarrier Effective for Axonal Outgrowth of Adult Neurons.* ACS Applied Materials & Interfaces, 2016. **8**(29): p. 18741-18753.
58. Choulli, F., et al., *Chemotherapy-related adverse effects with anthracycline and taxane-containing regimens in patients with localized Breast cancer: a descriptive study : Mohammed VI University Hospital, Medical Oncology Department, Marrakech, Morocco.* BMC Cancer, 2024. **24**(1): p. 17.
59. Rajkumar, S.V., *Multiple myeloma: Every year a new standard?* Hematol Oncol, 2019. **37 Suppl 1**: p. 62-65.
60. Ferlay J, E.M., Lam F, Laversanne M, Colombet M, Mery L, Piñeros M, Znaor A, Soerjomataram I, Bray F *Global Cancer Observatory: Cancer Today. Lyon, France:*

International Agency for Research on Cancer. 2024; Available from: Available from: https://gco.iarc.who.int/today.
61. Masarwi, M., et al., *Multiple Myeloma and Fatty Acid Metabolism.* JBMR Plus, 2019. **3**(3): p. e10173.
62. Hungria, V.T.M., et al., *New proteasome inhibitors in the treatment of multiple myeloma.* Hematol Transfus Cell Ther, 2019. **41**(1): p. 76-83.
63. Suraweera, A., K.J. O'Byrne, and D.J. Richard, *Combination therapy with histone deacetylase inhibitors (HDACi) for the treatment of cancer: achieving the full therapeutic potential of HDACi.* Frontiers in oncology, 2018. **8**: p. 92.
64. Mohan, M., A. Matin, and F.E. Davies, *Update on the optimal use of bortezomib in the treatment of multiple myeloma.* Cancer Manag Res, 2017. **9**: p. 51-63.
65. Luczkowska, K., et al., *Pathophysiology of drug-induce peripheral neuropathy in patients with multiple myeloma.* J Physiol Pharmacol, 2018. **69**(2).
66. Meregalli, C., et al., *Bortezomib-induced peripheral neurotoxicity in human multiple myeloma-bearing mice.* J Biol Regul Homeost Agents, 2015. **29**(1): p. 115-24.
67. Carozzi, V., A. Canta, and A. Chiorazzi, *Chemotherapy-induced peripheral neuropathy: what do we know about mechanisms?* Neuroscience letters, 2015. **596**: p. 90-107.
68. Eldridge, S., L. Guo, and J. Hamre III, *A Comparative Review of Chemotherapy-Induced Peripheral Neuropathy in In Vivo and In Vitro Models.* Toxicologic pathology, 2020: p. 0192623319861937.
69. Alé, A., A.A. Argyriou, and J. Bruna, *Sphingolipid metabolism products: potential new players in the pathogenesis of bortezomib-induced neuropathic pain.* Annals of translational medicine, 2018. **6**(Suppl 1).
70. Landowski, T.H., et al., *Mitochondrial-mediated disregulation of Ca2+ is a critical determinant of Velcade (PS-341/bortezomib) cytotoxicity in myeloma cell lines.* Cancer Res, 2005. **65**(9): p. 3828-36.
71. Piktel, E., et al., *Recent insights in nanotechnology-based drugs and formulations designed for effective anti-cancer therapy.* Journal of nanobiotechnology, 2016. **14**(1): p. 39.
72. Li, W.P., et al., *Formation of oligonucleotide-gated silica shell-coated Fe(3)O(4)-Au core-shell nanotrisoctahedra for magnetically targeted and near-infrared light-responsive theranostic platform.* J Am Chem Soc, 2014. **136**(28): p. 10062-75.
73. Zhou, Y., et al., *Mesoporous silica nanoparticles for drug and gene delivery.* Acta pharmaceutica sinica B, 2018. **8**(2): p. 165-177.
74. Pasqua, L., et al., *Mesoporous silica nanoparticles in cancer therapy: Relevance of the targeting function.* Mini reviews in medicinal chemistry, 2016. **16**(9): p. 743-753.
75. Lee, J.E., et al., *Multifunctional mesoporous silica nanocomposite nanoparticles for theranostic applications.* Accounts of chemical research, 2011. **44**(10): p. 893-902.
76. Nakamura, T., et al., *Mesoporous silica nanoparticles for 19 F magnetic resonance imaging, fluorescence imaging, and drug delivery.* Chemical science, 2015. **6**(3): p. 1986-1990.
77. Slita, A., et al., *Characterization of modified mesoporous silica nanoparticles as vectors for siRNA delivery.* Asian journal of pharmaceutical sciences, 2018. **13**(6): p. 592-599.
78. Cheng, C.A., et al., *Supramolecular Nanomachines as Stimuli-Responsive Gatekeepers on Mesoporous Silica Nanoparticles for Antibiotic and Cancer Drug Delivery.* Theranostics, 2019. **9**(11): p. 3341-3364.
79. Van De Donk, N.W. and S.Z. Usmani, *CD38 antibodies in multiple myeloma: mechanisms of action and modes of resistance.* Frontiers in immunology, 2018. **9**: p. 2134.
80. Krejcik, J., et al., *Daratumumab depletes CD38+ immune regulatory cells, promotes T-cell expansion, and skews T-cell repertoire in multiple myeloma.* Blood, The Journal of the American Society of Hematology, 2016. **128**(3): p. 384-394.

81. Giuliani, N. and F. Malavasi, *The immunotherapy in multiple myeloma: honoring the past, studying the present, and trying to design the future.* Frontiers in immunology, 2019. **10**: p. 1945.
82. Sarıman, M., et al., *Investigation of Gene Expressions of Myeloma Cells in the Bone Marrow of Multiple Myeloma Patients by Transcriptome Analysis.* Balkan medical journal, 2019. **36**(1): p. 23.
83. Morandi, F., et al., *CD38: a target for immunotherapeutic approaches in multiple myeloma.* Frontiers in immunology, 2018. **9**: p. 2722.
84. Nigro, A., et al., *Bortezomib-Loaded Mesoporous Silica Nanoparticles Selectively Alter Metabolism and Induce Death in Multiple Myeloma Cells.* Cancers (Basel), 2020. **12**(9).
85. Thawani, S.P., et al., *Bortezomib-associated demyelinating neuropathy--clinical and pathologic features.* J Clin Neuromuscul Dis, 2015. **16**(4): p. 202-9.
86. Argyriou, A.A., G. Iconomou, and H.P. Kalofonos, *Bortezomib-induced peripheral neuropathy in multiple myeloma: a comprehensive review of the literature.* Blood, 2008. **112**(5): p. 1593-9.
87. Farquhar-Smith, P., *Chemotherapy-induced neuropathic pain.* Curr Opin Support Palliat Care, 2011. **5**(1): p. 1-7.